KSCE Journal of Civil Engineering (2023) 27(10):4300-4322
DOI 10.1007/s12205-023-0390-8

pISSN 1226-7988, eISSN 1976-3808
www.springer.com/12205

Structural Engineering

Performance-based Analysis of Elastoplastic Rotational Behavior of Multi-cell Shaped Concrete-filled Steel Tubular Connection

Xi Chen[a], **Jianyang Xue**[b,c], **Hechao Li**[b], **Guangxu Tu**[d], **and Xin Lu**[e]

[a]*Dept. of Civil Engineering, Henan University of Science and Technology, Luoyang 471000, China*
[b]*Dept. of Civil Engineering, Xi'an University of Architecture and Technology, Xi'an 710055, China*
[c]*Key Lab of Structure and Earthquake Resistance of the Ministry of Education, Xi'an, University of Architecture and Technology, Xi'an 710055, China*
[d]*Shaanxi Metallurgical Design & Research Institute Co., Ltd., Xi'an 710018, China*
[e]*China United Engineering Corporation Limited, Hangzhou 310051, China*

ARTICLE HISTORY

Received 22 March 2022
Revised 30 April 2023
Accepted 13 June 2023
Published Online 15 August 2023

KEYWORDS

Performance-based analysis
Connection
Bending rigidity
Multi-cell shaped columns
Steel beams
Plastic hinge

ABSTRACT

Experimental and theoretical research on the rotational behavior of Multi-cell shaped concrete-filled steel tubular (MCFST) connection under low-period cyclic load is performed. The experimental results showed that the design parameters had significant effects on the elastic rotational stiffness of the connection, and affected the sequence and position of the plastic hinges appearance at the column and beam ends. Furthermore, the damage mechanism of the plastic hinge lines is obtained, and the simultaneous yielding for the plastic hinges results in the rapid increase of the beam end rotation. In order to handle the problem with irregular geometry boundary and uneven distribution of tightening-ring stresses a differential element of an unified material is proposed considering the effective tightening-ring stresses of special-shaped steel tube on confined concrete, which can be used to analyse the whole mechanical and damage performance of the connection. Combining unified design theory and experimental results, the calculation for the elastic bending rigidity of the connection is obtained. Finally, the moment-rotation relation model of the connection is proposed by regression analysis on experimental results, and the theoretical results are observed to agree well with the experimental results.

1. Introduction

Special-shaped concrete-filled steel tubular frame structures have been proposed and widely applied in civil infrastructures due to their supe-riority of architectural functions, efficient use of both the materials, and saving in construction time due to the elimination of formwork. Compared with special-shape reinforced concrete column frame structure, they are also more advantageous in terms of seismic performance, load capacity, and ductility according to the research conducted by Yang et al. (2022) and Abbas et al. (2021). In mechanical property researched by Liu et al. (2023), compared to the rectangular and circular CFST columns, the load-bearing performance and overall stability performance of the irregular-shaped CFST columns are more complicated and involve much more design parameters. The shear resistance of special-shaped concrete-filled steel tubular connection was studied by Chen et al. (2023). The seismic performance of T-shaped multi-cell CFST columns to cold-formed U-shaped steel-concrete composite connection was studied by Cheng et al. (2023).

The research conducted by Zheng and Pengsong Lai (2020) on T-shaped concrete-filled steel tubular (CFST) columns showed that the initial section flexural stiffness utilizing the full flexural stiffness of the steel and a reduced stiffness provided by the core concrete had a large deviation from the test results for the multi-cell CFST specimens. The mechanical performance of hexagonal multi-cell CFST stub columns under axial compression was numerically investigated by Zhang et al. (2019). To reflect the confinement effect of the steel tube, a confinement factor was calculated individually for each concrete cell according to the geometric and material characteristics of the surrounding subpanel plates. According to the research by Yang et al. (2015), the uniformly distributed lateral pressure of T-shaped CFST columns was defined by the confinement effectiveness coefficient, which was the ratio of the area of the non-stiffened core concrete to the

CORRESPONDENCE Xi Chen chenximy2018@haust.edu.cn Dept. of Civil Engineering, Henan University of Science and Technology, Luoyang 471000, China

area of the core concrete. According to unified theory proposed by Zhong (2006), the CFST was looked as an unified body composed of a new composite material. The behaviors of various forms of CFST members under axial compression by use of equivalent circular members including the solid and hollow cross sections were obtained. Based on the research of the composite behaviors of the unified material, a serious composite characteristics indexes were derived. The bearing capacities and deformations for the members were calculated by use of the composite indexes.

The experimental study conducted by Shehab and Ekmekyapar (2021) demonstrated that the presence of the flange portion of steel beam through CFST column connections contributed significantly to the moment and rotation capacity of the connections. The research conducted by Qin et al. (2015a, 2015b) showed that the bending failure of CFST connection accorded with yielding line mechanism of column flanges, and the distortion of the plastic hinges had a great influence on the deformation of the connection. The yield line analysis method for estimating the strength of different rectangular hollow section connections was proposed by Cao et al. (1998).

The moment-rotation relation models are indispensable in the connection design, and require experimental or simulation data to fit the shape parameters of the moment-rotation curves and the physical parameters of analytical expression of the models. Zhou et al. (2019) proposed a practical analytical model for the moment-rotation relation of CFST connection, considering the yield line failure modes of the column flange and the endplate, based on the dimension parameters and the material properties of the connection. Wang et al. (2008) studied the behaviour of CFST connections and found that there was an initial elastic response in the measured moment versus relative beam-column rotation curves, followed by inelastic behaviour with gradually decreasing stiffness. The analytic expression of the moment versus relative beam-column rotation curves of ring board CFST connection was derived by Khndada and Geschwindner (1997).

The parametric study of the resistance of special-shaped CFST columns conducted by Liu et al. (2020) showed that steel-to-concrete ratio, steel yield strength and column limb width-to-thickness ratio had obvious influences on the flexural resistances of the columns. Research results showed that the mono column of the columns worked together well, and an increase of axial compression ratio increased the stiffnesses of the columns, and an increase of column section length to width ratio led to a decrease of the stiffnesses. Liu et al. (2019) studied the properties of slender L-shaped CFST column, it was found that the load-strain curves decreased and entered a horizontal yielding stage, which indicated that some steel tubes were under plastic state. The object of the study in unified design theory proposed by Zhong (2006) was CFST members with single limb and symmetrical section, but the MCFST column was composed of several limbs, and the cross section of the column was symmetrical or asymmetrical, and the cell steel tubes were connected to form an unity by welding, which made the limbs work together.

The mechanical behavior and the damage mechanism of MCFST connection at material level play a significant role in rotational behavior of the connection. However, the research on the rotational behavior of the connection from the material level is still blank. As the result of special-shaped cross section of the specimens, the tightening-ring stresses distribution of the special-shaped steel tube are uneven, and the geometry boundary of the stresses are irregular. The tightening-ring stresses redistribution caused by the deformation coordination of the limbs makes the stress analysis more complicated. And the damage mechanism of the connection at elastoplastic stage is still blank, and the performance-based analysis method of the elastoplastic rotational behavior is needed to study at present. In this paper, based on the unified design theory of CFST, through introducing a differential element of the unified material, the above problems, for example, the uneven distribution of stresses and the irregular boundary caused by the design parameters of the cross sections and the interaction between the limbs, can be effectively solved. Based on the unified design theory and experimental research, the method of calculation for the elastic bending rigidity of the connection is obtained. By experimental results analysis, the rules of the generation and the development of plastic hinges at the ends of the column and beam are deduced from the material level. Furthermore, the damage mechanism of plastic hinge lines is obtained, and the analysis model of the simultaneous yielding for the plastic hinge lines is derived. Finally, the moment-rotation relation model is proposed by using regression analysis on the experimental results, and the theoretical results are observed to agree well with the experimental results.

2. Experimental Program

2.1 Specimen Design and Fabrication

MCSFT connections under low-period cyclic lateral loads and

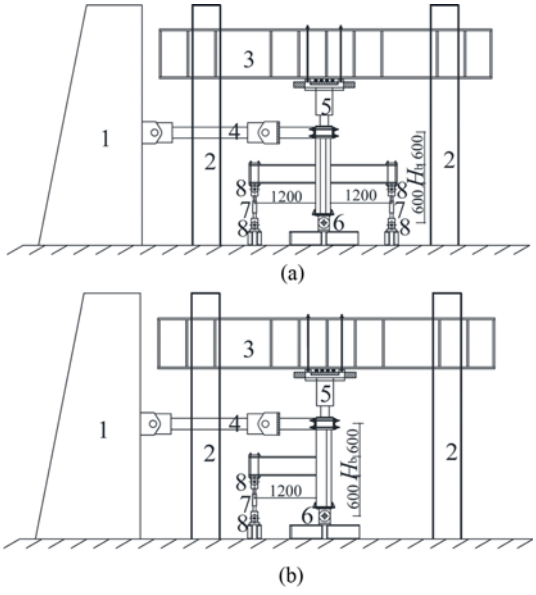

Fig. 1. Test Setup: (a) S+ Specimens, (b) ST and SL Specimens (1. reaction wall, 2. reaction frame, 3. anti-force beam, 4. electro-hydraulic servo systems, 5. hydraulic jacks 6. unidirectional hinged bearing at column end, 7. force sensor, 8. unidirectional hinged bearing at beam end)

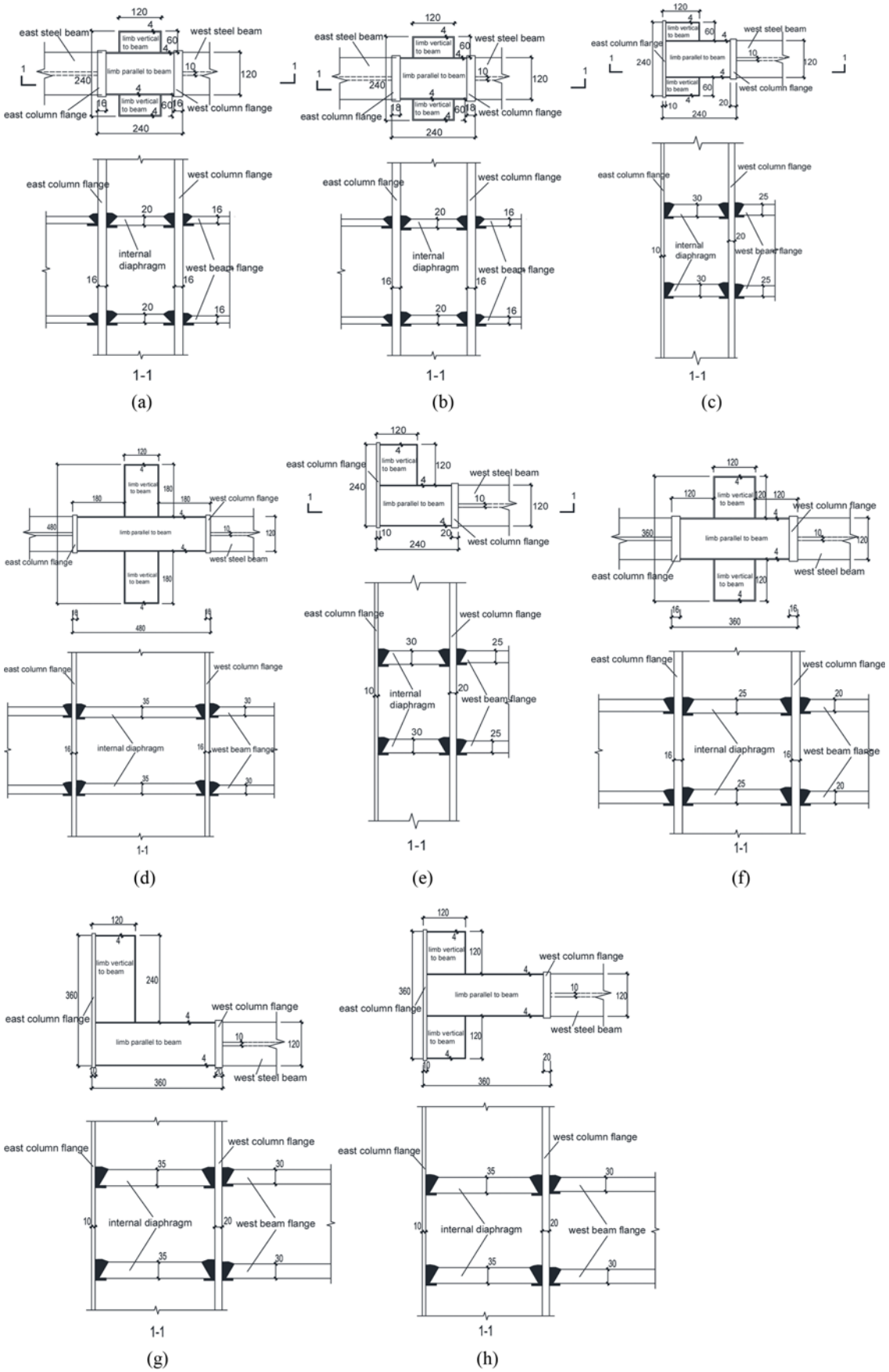

Fig. 2. Details of Specimens: (a) S+1 and S+2, (b) S+3, (c) ST1, (d) S+4, (e) SL1, (f) S+5, (g) SL2, (h) ST2

constant axial compressive loads to investigate the elastoplastic behavior of the joint were tested shown in Fig. 1. The loading device in the test was shown in Fig. 1. The specimens were designed with half-scale. The design parameters included the cross-sectional shapes (L, T and +), the height to thickness ratio of the column section β and axial compression ratio n of the column, where β is defined as $\beta = L_w/H_{w2}$, and n is defined as $n = N/[\sigma_{cB}(A_c + \alpha_E A_s)]$.

Figure 2 presents details of the test specimens. The specimens were designed with all-welded internal diaphragm,as recommended by the design regulations (CECS159:2004, 2004).

2.2 Material Properties

Standard steel tensile specimens were fabricated and tensile tests were conducted according to the relevant Chinese National Standard (GB/T 228.1-2010, 2010). According to the experimental results of the steel tensile specimens, the measured stress-strain relationship of the samples conformed to the trilinear model for the stress-strain relation proposed by Patel and Chen (1984) as shown in Fig. 3. α_{s1} and α_{s2} are defined as $\alpha_{s1} = \frac{E_s'}{E_s}$ and $\alpha_{s2} = \frac{E_s''}{E_s}$, respectively, where E_s' and E_s'' are the second and the third modulus of steel material, respectively.

Table 1 reports the details of the steel plate tensile coupons.

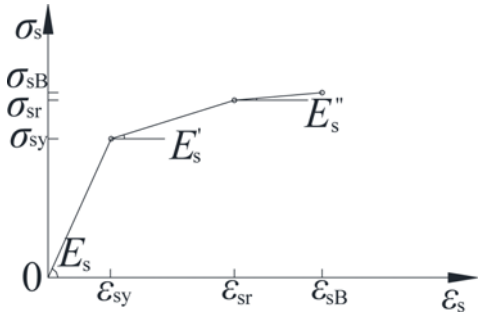

Fig. 3. Trilinear Model for Axial Stress-Strain

Table 1. Data of Tensile Coupons

Thickness (mm)	4	10	16	18	20
Steel type	Q235	Q345	Q345	Q345	Q345
Yield stress σ_{sy} (N/mm^2)	284	354	354	378	398
Ultimate stress σ_{sB} (N/mm^2)	419	486	524	540	577
Elastic Modulus E_s (10^5MPa)	2.13	2.06	1.96	1.93	1.86
α_{s1}	0.1062	0.0290	0.0428	0.0079	0.0557
α_{s2}	0.0285	0.0040	0.0048	0.0016	0.0040
Average of Compressive Strength of concrete σ_{cB} (MPa)	43				

The material characteristics of the steel plates are summarized by Chen et al. (2023). Nine 150 × 150 × 150 mm concrete cubes were sampled and tested. All standard concrete cubes were fabricated, sampled and tested according to the relevant Chinese National Standard (GB/T 50081-2002, 2002). Table 2 reports the concrete proportion.

2.3 Loading Scheme and Measurement Devices

In order to understand how the connections enter into the elasto-plastic state a mixed force-displacement loading system is introduced as shown in Fig. 4. When the rigidities of the specimens in the lateral force-displacement hysteretic curves obviously decreased, and the material of the limbs reached the yield strength, the load displacement of the specimens reached the yield displacement Δ_y. Then the loading system started to control the monotonic loading. Testing was conducted until the lateral loading resistances decreased below 85% of the maximum of the resistances.

In order to investigate the stress state of the plastic hinges at the column ends (hereinafter referred to as CE) and at the beam ends (hereinafter referred to as BE), the strain gauges were arranged to measure the strains of the flanges of CE and BE. The strain gauges were placed in the joint to measure the strains of the steel webs as shown in Fig. 5. Fig. 6 showed the instrumentation layout, where W is the displacement gauge, and S is the dial gauge of which the measuring range is 10 mm. W1 and W2 are used to measure the horizontal displacements of the column top and the joint, respectively. The rotation θ_b of BE can be obtained by S1 and S2, and the rotation θ_b of BE can be given as follows:

$$\theta_b = (\Delta_2 - \Delta_1)/150\,, \tag{1}$$

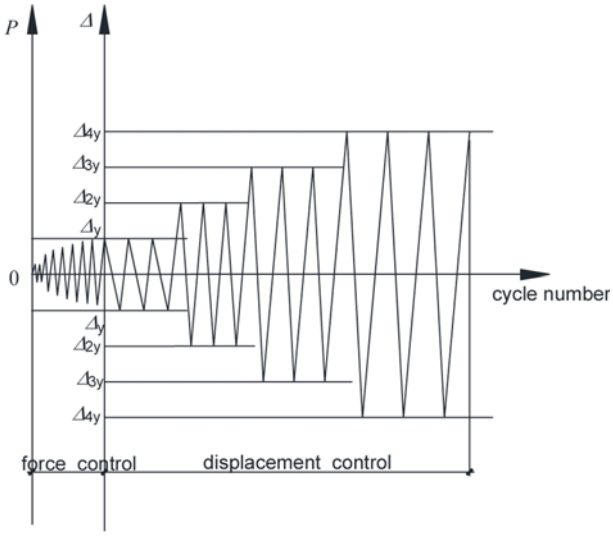

Fig. 4. Loading System of Specimens

Table 2. Data of Concrete Proportion

Materials composing of concrete	Cement	Fly ash	Sand	Pisolite	Admixture	Water
Mass of component materials of concrete per cubic meter (kg)	340	80	632	1135	8.6	170

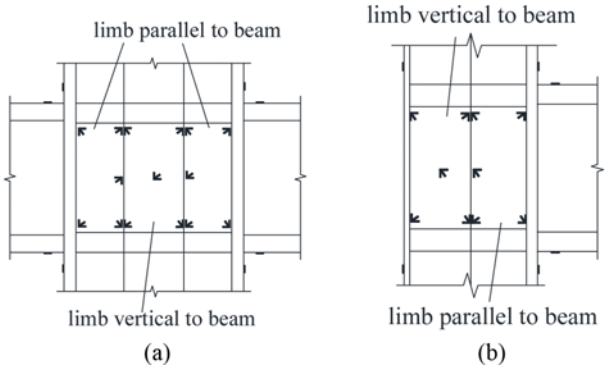

Fig. 5. Layout of Strain Gauges for Specimens: (a) S+ Specimens, (b) ST and SL Specimens

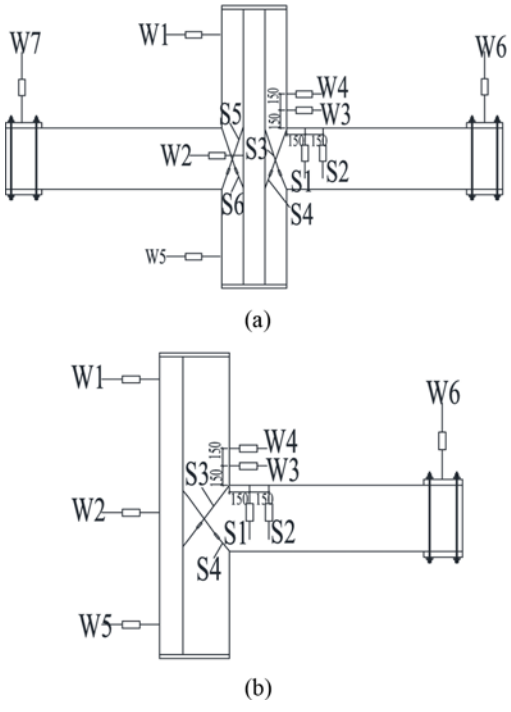

Fig. 6. Instrumentation Layout: (a) S+ Specimens, (b) ST and SL Specimens

where Δ_1 and Δ_2 are the displacements measured by dial gauges 1and 2 respectively. The rotation θ_c of CE can be obtained by W3 and W4, and the rotation θ_c of CE can be given as follows:

$$\theta_c = (\Delta_4 - \Delta_3)/150 , \tag{2}$$

where Δ_3 and Δ_4 are the displacements measured by displacement gauges 3 and 4 respectively.

3. Failure Process and Performance-Based Analysis of Lateral Moment-Rotation Hysteretic Curves

According to the previous research results by Han et al. (2009), it is assumed that the rotations of CE and BE adjacent the joint are mainly caused by the bending moment of the joint M_j, and the calculation of the bending moment M_j needs to consider the second order effect and is obtained as follows:

$$M_j = V \cdot (H/2 - H_b/2) + N \cdot (\delta_u - \delta_m) , \tag{3}$$

where V is the horizontal load on the top of the column, N is the axial pressure force on the top of the column, H is the height of the column, δ_u is the horizontal displacement of the column, δ_m is the horizontal displacement of the joint, δ_u and δ_m are measured by the displacement gauges 1 and 2. The relative rotation θ_r between CE and BE can be obtained as follows:

$$\theta_r = \theta_b - \theta_c . \tag{4}$$

In order to obtain the variety regulation of the bending rigidity of the connection at the elastoplastic stage, the performance of $M_j - \theta_c$, $M_j - \theta_b$ and $M_j - \theta_r$ hysteretic curves is analyzed as shown in Fig. 7.

Figure 7 depicts the bending moment M_j of the joint-θ_c, θ_b and θ_r hysteretic curves.

In Fig. 7, the state point I indicated that the strains measured by the strain rosettes on the joint reached the yield point for the first time, and the specimens entered the elastic-plastic phase. At stage O-I, M_j-θ_c, M_j-θ_b and M_j-θ_r hysteretic curves for specimens S+1, S+2, S+3 and SL1 generally exhibit a linear relationship. This indicates that the joint, CE and BE of specimens S+1, S+2, S+3 and SL1 work within the elastic range. M_j -θ_c hysteretic curves of specimens S+4, S+5, ST1, ST2, and SL2 also follow a linear relationship, which indicates that CE of specimens S+4, S+5, ST1, ST2, and SL2 work within the elastic range. The large slipping of rotations θ_b of specimens S+4 and S+5 is observed, which indicates that the large plastic deformations of BE of specimens S+4 and S+5 occur. Moreover, the small slipping of rotations θ_b of specimens ST1, ST2, SL1 and SL2 is also observed, which indicates that the small plastic deformations of BE of specimens ST1, ST2, SL1 and SL2 occur.

At state point II the stiffnesses of the M_j-θ_c, M_j-θ_b and M_j-θ_r hysteretic curves for all specimens exhibit a significant reduction, and the strains of the steel webs of the limb parallel to the beam measured by over ninety percent of strain rosettes exceed the yield point. After state point II, θ_b of specimen S+5 went beyond the measuring range, soθ_b of specimen S+5 was invalid. During the loading process, the stresses of the steel webs of the limbs vertical to the beam of specimens S+4, S+5, SL1 and SL2 did not exceed the yield point. This was also true for the corner of the steel webs of the limbs vertical to the beam of specimen ST2.

The shape of the M_j-θ_c hysteretic loops curves of the specimens S+1, S+2, S+3, ST1 and SL1 is similar to the M_j-θ_r hysteretic curves of those. This is because the plastic deformation of BE of the specimens is far less than that of CE. The plastic deformation of BE of the specimens exerts minimal effort on θ_c, and θ_r at the plastic damage stage is controlled by θ_c.

The state point III indicated that the specimens achieved both the positive and negative limit state. At stage II-III the shape of the envelope of the M_j-θ_b hysteretic curves of specimen S+1 is close to that at stage O-I as shown in Fig. 7(b). After state point II, the plastic deformation of θ_r of specimen S+3 continuously increases with the increase of the rotation of BE and CE, and consequently the

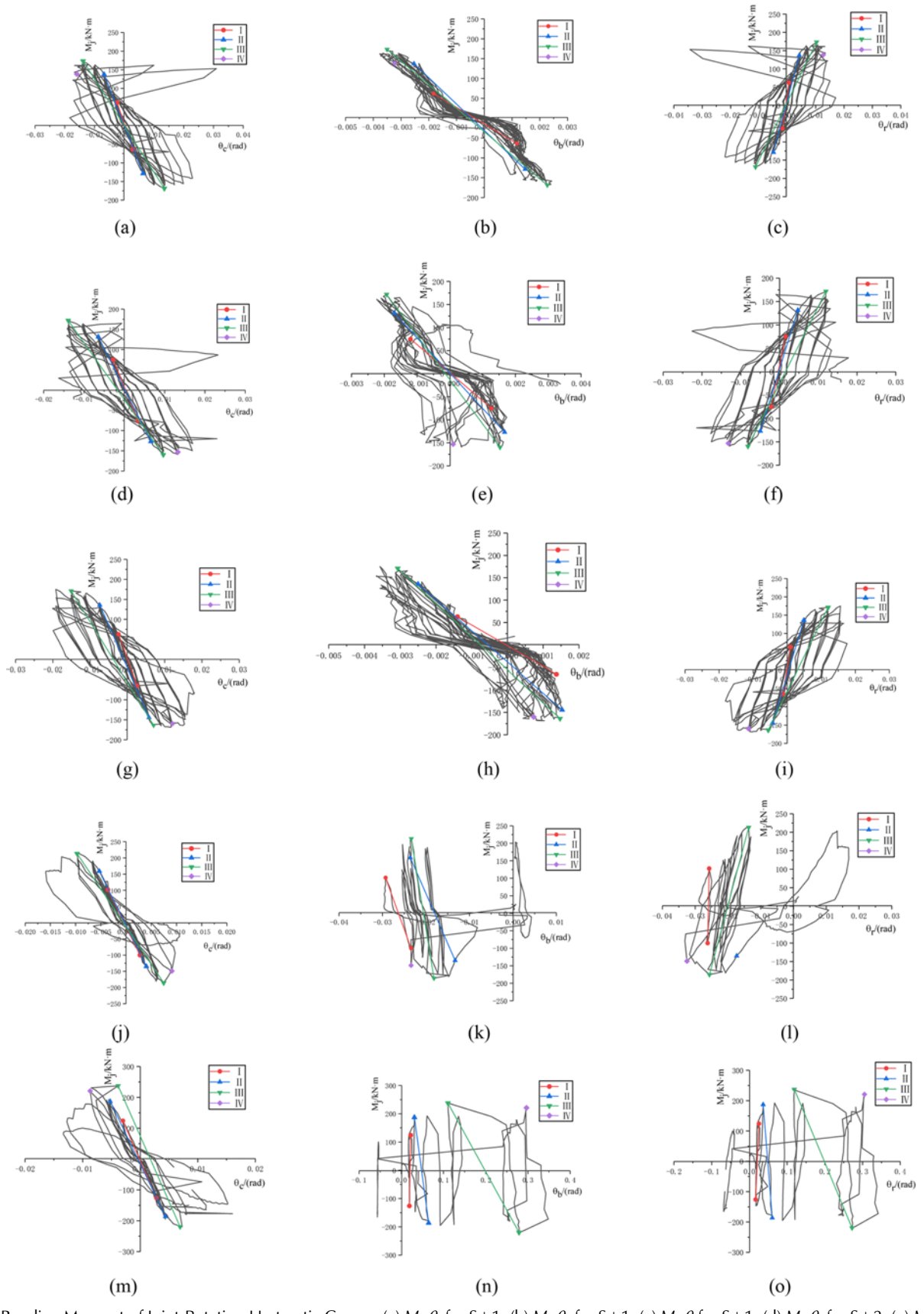

Fig. 7. Bending Moment of Joint-Rotation Hysteretic Curves: (a) M_j-θ_c for S+1, (b) M_j-θ_b for S+1, (c) M_j-θ_r for S+1, (d) M_j-θ_c for S+2, (e) M_j-θ_b for S+2, (f) M_j-θ_r for S+2, (g) M_j-θ_c for S+3, (h) M_j-θ_b for S+3, (i) M_j-θ_r for S+3, (j) M_j-θ_c for S+4, (k) M_j-θ_b for S+4, (l) M_j-θ_r for S+4, (m) M_j-θ_c for S+5, (n) M_j-θ_b for S+5, (o) M_j-θ_r for S+5

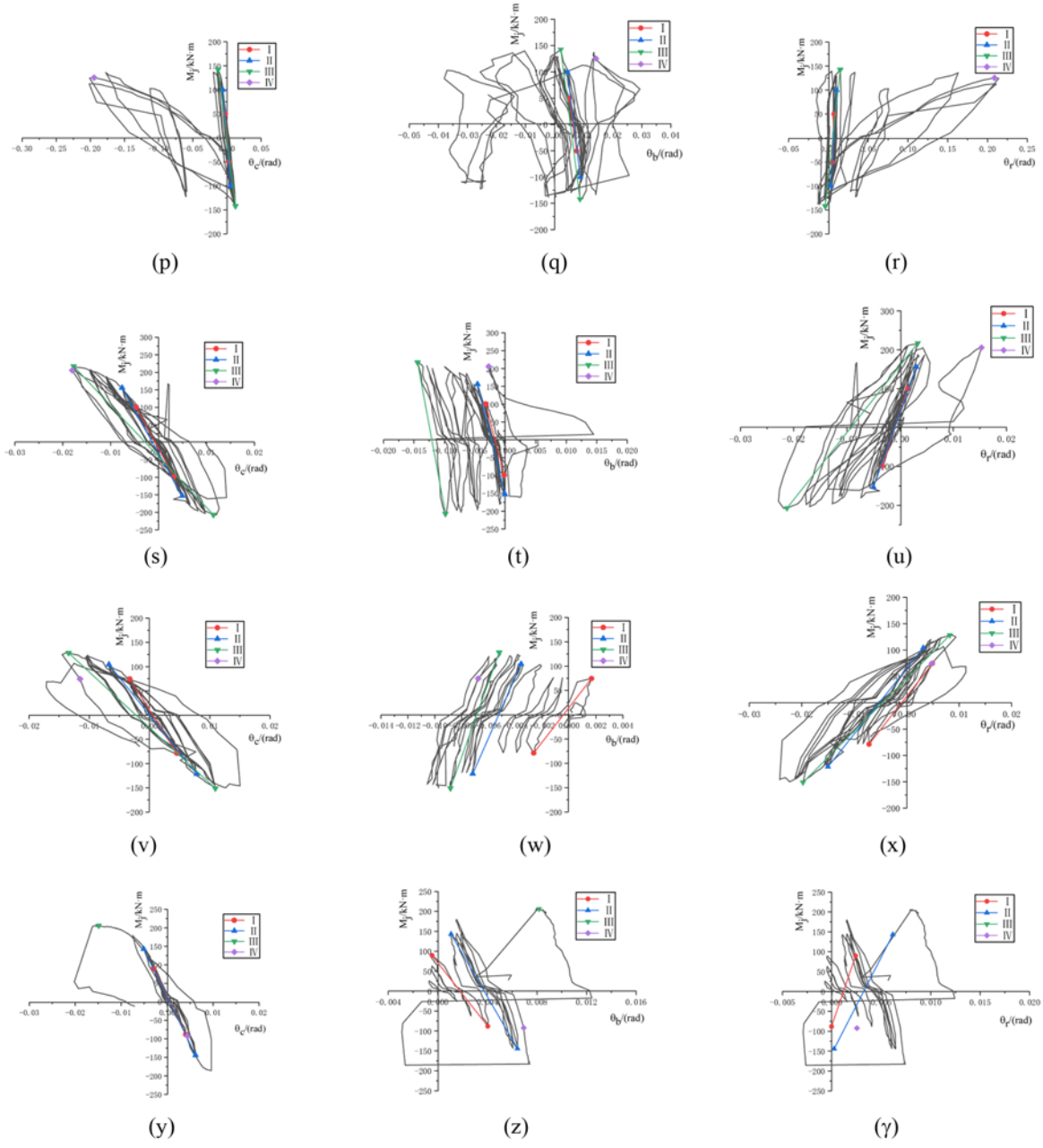

Fig. 7. (continued): (p) M_j-θ_c for ST1, (q) M_j-θ_b for ST1, (r) M_j-θ_r for ST1, (s) M_j-θ_c for ST2, (t) M_j-θ_b for ST2, (u) M_j-θ_r for ST2, (v) M_j-θ_c for SL1, (w) M_j-θ_b for SL1, (x) M_j-θ_r for SL1, (y) M_j-θ_c for SL2, (z) M_j-θ_b for SL2, (γ) M_j-θ_r for SL2

hysteresis loops of the specimen S+3 are full as shown in Fig. 7(i). The state point IV indicated that the weld connecting the web and the flange of the limb parallel to the beam cracked in the region close to the internal diaphragm and steel beam flange as shown in Fig. 8. And the cracks widened and extended in the vertical direction.

4. Damage Mechanism of Rotational Behavior of Joint

4.1 Performance-Based Analysis of Elastoplastic Stress of Column and Beam End Flange

In order to accurately analysis the distribution and state of the stresses in BE and CE, BE and CE are divided into regions R1, R2, R3, R4, R5, R6, R7 and R8 shown in Fig. 9. Based on the trilinear model for axial stress-strain demonstrated in Fig. 3, the stresses in regions R1, R2, R3, R4, R5, R6, R7 and R8 are calculated using the strain gauge measurements. The analysis of the distribution and development of the stress is obtained, which reveals from the material level the basic causes for the elastoplastic rotational behavior of the joint.

Figure 10 presents the stresses of BE and CE flanges at measuring points-θ_r envelope curves.

Figure 10(a) shows σ-θ_r envelope curves for specimen S+1. At state point II, the stresses calculated by all measured strains in

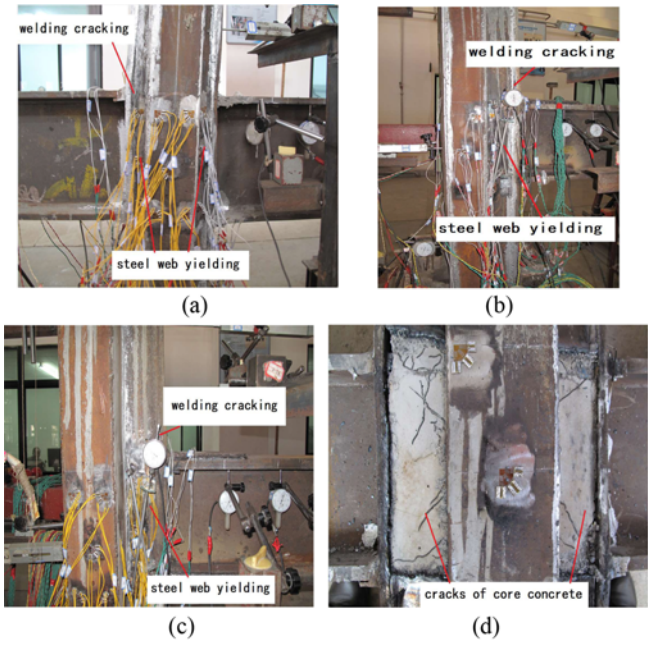

Fig. 8. Failure of Joint: (a) Failure of Steel Tubular of Specimen S+2, (b) Failure of Steel Tubular of Specimen ST1, (c) Failure of Steel Tubular of Specimen SL1, (d) Failure of Confined Concrete of Specimen S+4

R4 exceed the yield point. At stages II-III, increasing θ_r of the connection does not have a great impact on the stresses in R4. Following state point III, a horizontal line segment on the curves of the stresses in R4, R1 and R8 under negative rotation is observed. At state point IV, the stresses in R1and R8 reach the yield state.

Figure 10(b) shows σ-θ_r envelope curves for specimen S+2. When θ_r is 0.002 shown in state point A of Fig. 10(b), the stresses in R8 and R6 begin to yield. When θ_r is 0.0034, the stresses in R3 also begins to yield. When θ_r is -0.0049 shown in state point B of Fig. 10(b), the stress in R4 begins yielding. Increasing θ_r at stage A-III has a limited impact on the stress in R8. This is also true for the stress in R5 under the negative rotation at stage I-III, and the stresses in R8 under the negative rotation at stage B-III. At state point III, the stresses calculated by all measured strains in R3, R4, R5, R6, R7 and R8 exceed the yield point. Moreover, When θ_r is -0.0177 shown in state point C of Fig. 10(b), the stresses in R1 and R2 reach the yielded state.

Figure 10(c) shows σ-θ_r envelope curves for specimen S+3. When θ_r is 0.0021 shown in state point A of Fig. 10(c), the stress in R3 begins to yield. When θ_r is 0.0023 shown in state point B of Fig. 10(c), the stresses calculated by all measured strains in R3 exceed the yield point, and the stresses in R5 begin to yield. Following state point II, a horizontal line segment is observed on the curves of the stress in R3. At state point II, the stresses determined by all measured strains in R4 and R7 exceed the yield point. When θ_r is -0.0152 and the moment is decreased to -149 kN·m, the stress in R1begins to yield, while the stresses calculated by all measured strains in R5 reach the yielded state. When θ_r is 0.0154 shown in state point C of Fig. 10(c), the stresses calculated by all measured strains in R6 exceed the yield point.

Figure 10(d) shows σ-θ_r envelope curves for specimen S+4. When θ_r is -0.0222 shown in state point A of Fig. 10(d), the stress in R3 begins to yield, which is also true for the stresses in R3 and R5 at state point III. When θ_r is -0.0244 shown in state point B of Fig. 10(d), the stress in R6 begins to yield, while the stresses determined by all measured strains in R7 exceed the yield point. Following state point B and under positive and negative bending moments tensile and compressive stresses are generated respectively, and the direction of the bending moment and the stresses changes alternately. θ_r is 0.0168 shown in state point C of Fig. 10(d). For state phase BC, increasing θ_r results in the approximate centering of the stress curves on the θ_r axis,

and the direction of the stresses changes alternately along the positive and negative bending moments. Thus, the stress enveloping curve can be approximated by the horizontal line as shown in Fig. 10(d). At state point II, the stress in R8 begins to yield, while the stresses calculated by all measured strains in R6 exceed the yield point. When θ_r is -0.030, and the moment is decreased to 156 kN·m, the stresses calculated by all measured strains in R8 exceed the yield point. When θ_r is 0.0168, and the moment is reduced to 157 kN·m, the stress in R2 begins to yield. And when

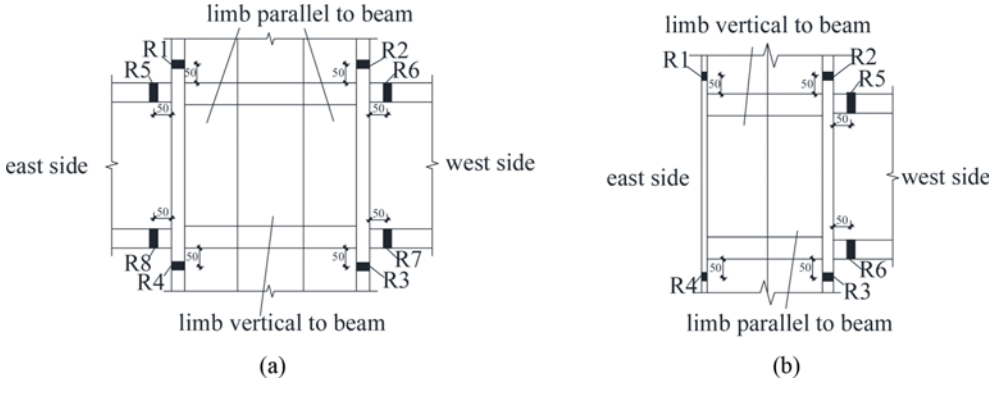

Fig. 9. Decomposition Method for BE and CE: (a) S+ Specimens, (b) ST and SL Specimens

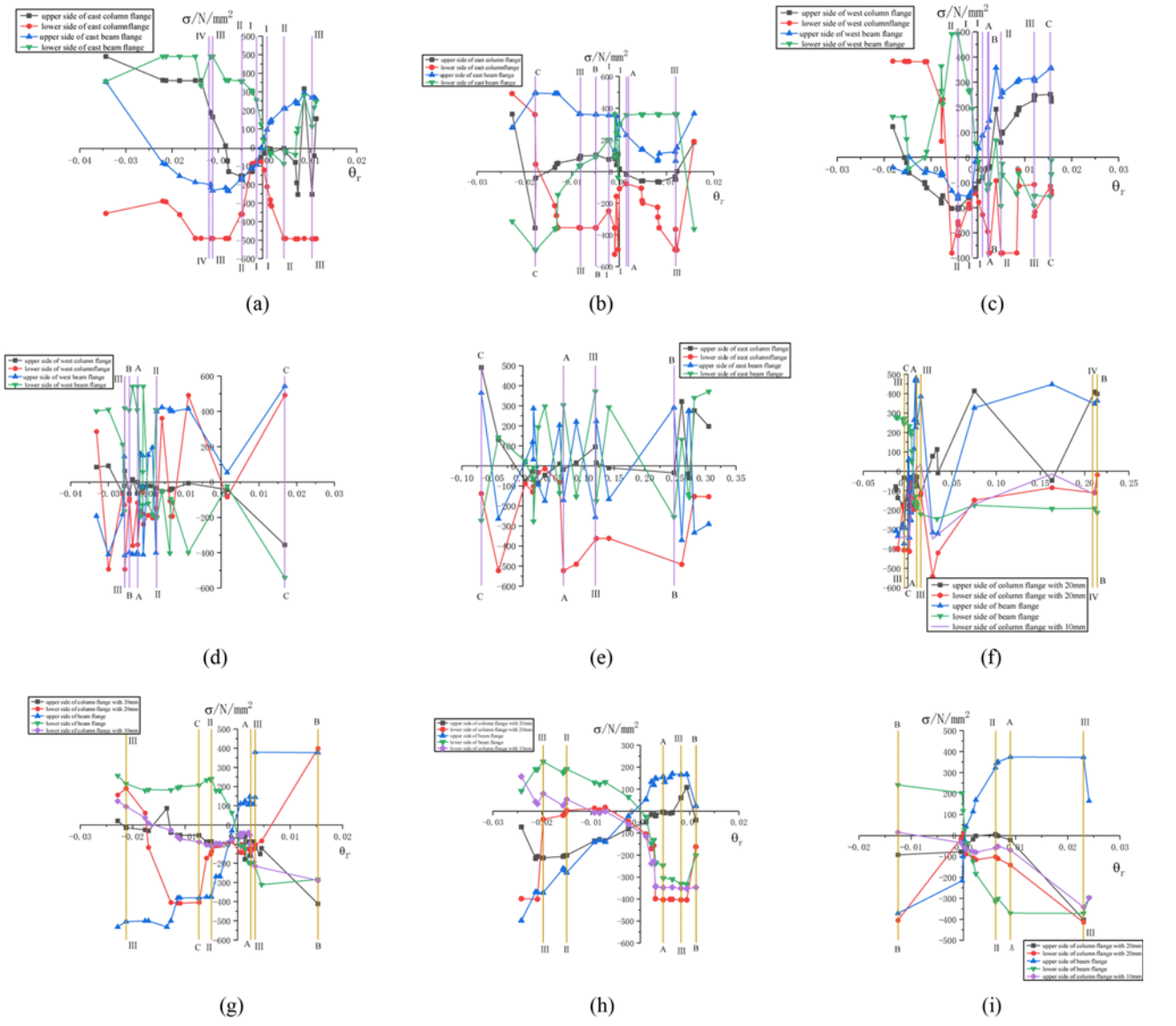

Fig. 10. Stress σ of BE and CE Flanges at Measuring Points - θ_r Envelope Curves: (a) S+1, (b) S+2, (c) S+3, (d) S+4, (e) S+5, (f) ST1, (g) ST2, (h) SL1, (i) SL2

θ_r is -0.0088, and the moment is decreased to -42 kN·m, the stresses calculated by all measured strains in R1 exceed the yield point.

Figure 10(e) shows σ-θ_r envelope curves for specimen S+5. When θ_r is 0.0667 shown in state point A of Fig. 10(e), the stress in R4 begin to yield. When θ_r is 0.1414, the stress in R6 begins to yield. At state point III, the stresses determined by all measured strains in R4 and R6 exceed the yield point, while the stresses in R3 and R8 begin to yield. When θ_r is 0.2484 shown in state point B of Fig. 10(e), the stresses in R2 and R5 begin to yield. Following state point B, increasing θ_r results in the approximate centering of the curves on the θ_r axis. Moreover, the direction of the stresses changes alternately along the positive and negative bending moment, and the enveloping curve of the stress can be approximated by a horizontal line. When θ_r is -0.068 shown in state point C of Fig. 10(e), the stress in R1 begins to yield, and the stresses calculated by all measured strains in R5 exceed the yield point. When θ_r is 0.0175, and the moment is decreased to -143 kN·m, the stresses calculated by all measured strains in R1 and R3 exceed the yield point.

Figure 10(f) shows σ-θ_r envelope curves for specimen ST1. When θ_r is 0.0102 shown in state point A of Fig. 10(f), the stress in R5 begins to yield. When θ_r is -0.0036 shown in state point C of Fig. 10(f), this is also true at state point C for the stresses in R4. At state point III, the stresses determined by all measured strains in R1 and R5 exceed the yield point, stress of R3 begins to yield. When θ_r is 0.2142 shown in state point B of Fig. 10(f), the stresses calculated by all measured strains in R2 exceed the yield point. When θ_r is 0.0021, and the moment is decreased to -134 kN·m, the stresses calculated by all measured strains in R4 exceed the yield point. When θ_r is 0.0282?and the moment is reduced to -111 kN·m, the stresses calculated by all measured

strains in R5 and R6 exceed the yield point.

Figure 10(g) shows σ-θ_r envelope curves for specimen ST2. When θ_r is 0.0025 shown in state point A of Fig. 10(g), the stresses in R5 and R6 begin to yield. At state point II the stresses calculated by all measured strains in R5 exceed the yield point. θ_r is 0.0153 shown in state point B of Fig. 10(g). As θ_r of the connection increases at stages III-B and II-III, the stresses in R5 and R6 generally remain the same. This is also true for the positive stresses in R5 and R6 at stage II-III. When θ_r is -0.0074 shown in state point C of Fig. 10(g), the stresses determined by all measured strains in R3 exceed the yield point. When θ_r is 0.0043, the stresses calculated by all measured strains in R6 exceed the yield point. At state point III, the stress in R2 begins to yield. This is also true for the stress in R4 at state point IV.

Figure 10(h) shows σ-θ_r envelope curves for specimen SL1. When θ_r is 0.0046 shown in state point A of Fig. 10(h), the stresses in R4 and R3 begin to yield, and at the state point, the stress in R5 begins to yield. Increasing θ_r of the connection at stage A-III does not have a great impact on the negative stresses in R4 and R3. θ_r is 0.0113 shown in state point B of Fig. 10(h). At state point III the negative stresses calculated by all measured strains in R5 exceed the yield point, while at state point B the stress in R2 begins to yield.

Figure 10(i) shows σ-θ_r envelope curves for specimen SL2. At state point II the stresses of R5 and R6 begin to yield. θ_r is 0.009 shown in state point B of Fig. 10(i). At state point B, the stresses calculated by all measured strains in R5 and R6 exceed the yield point. As θ_r of the connection increases at the stage II-III, the stresses in R5 and R6 remain largely the same. When θ_r is -0.0125 shown in state point C of Fig. 10(i), the stress in R3 begins to yield. At state point III, the stresses in R1 and R2 begin to yield.

4.2 Performance-Based Analysis Model for plastic Hinges of BE and CE Flanges

According to the above conclusion, when the stresses calculated

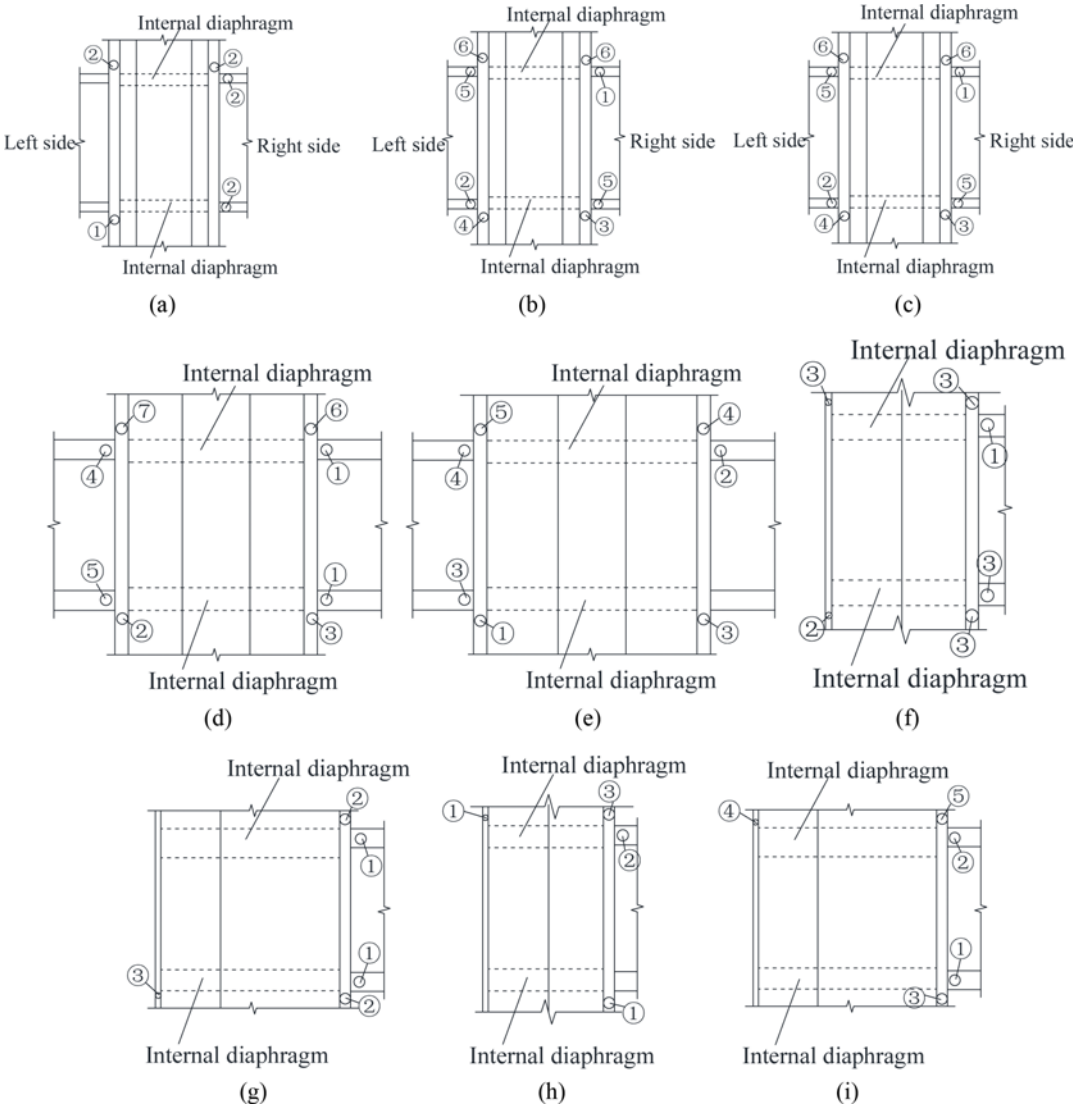

Fig. 11. Produce Order of Plastic Hinges for Flanges of BE and CE: (a) S+1, (b) S+2, (c) S+3, (d) S+4, (e) S+5, (f) ST1, (g) ST2, (h) SL1, (i) SL2

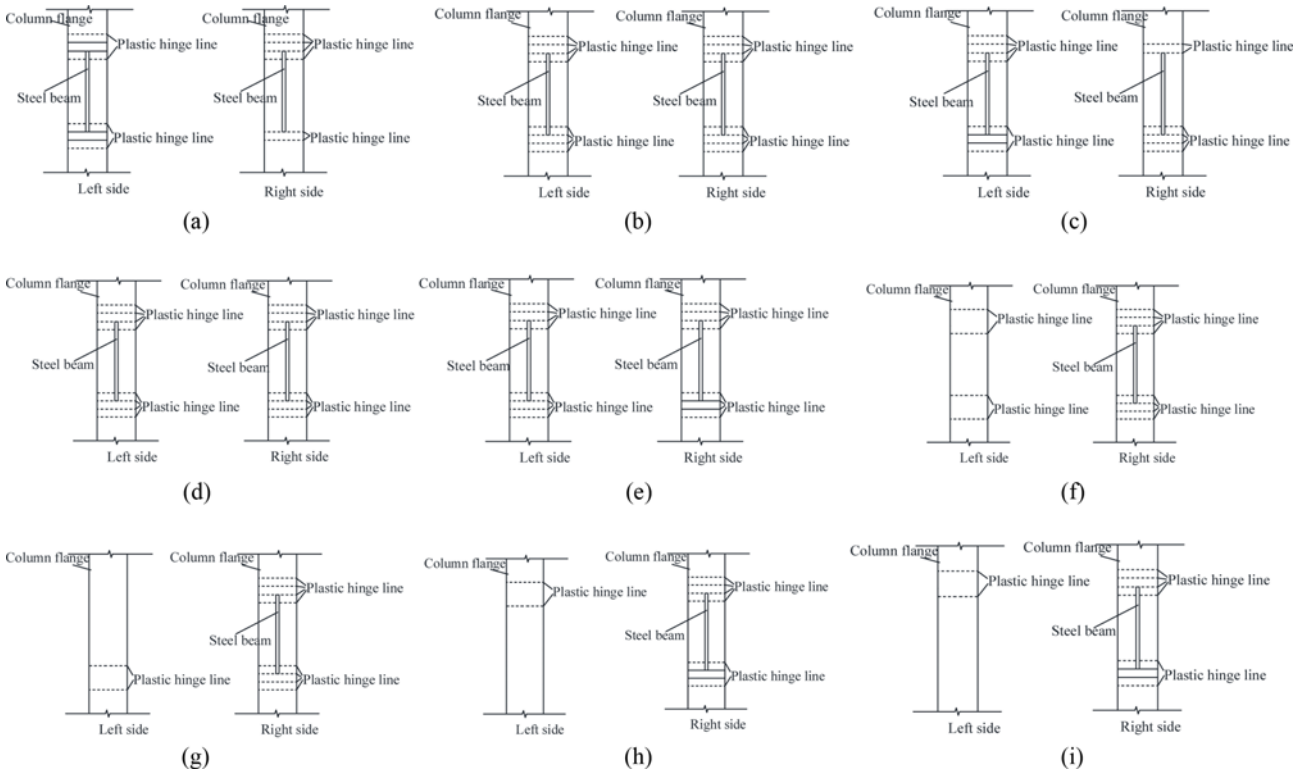

Fig. 12. Analysis Model of Plastic Hinge Lines for Flanges of BE and CE at Ultimate State: (a) S+1, (b) S+2, (c) S+3, (d) S+4, (e) S+5, (f) ST1, (g) ST2, (h) SL1, (i) SL2

by the strains in R1, R2, R3, R4, R5, R6, R7 and R8 begin to yield, it is indicated that the plastic hinges for the flanges of BE and CE start to form. When the stresses calculated by all measured strains in R1, R2, R3, R4, R5, R6, R7 and R8 exceed the yield point, it is indicated that the plasticity of the plastic hinges develops fully. The produce order of plastic hinges in BE and CE is shown in Fig. 11. From Fig. 11, it is seen that the produce orders of the plastic hinges vary with the design parameters of the specimens.

As shown in Fig. 10, when the stress enveloping curve is approximated by the horizontal line, it is indicated that the plastic hinges bear the load on the joint, and the deformation of the plastic hinges is produced, which is the main cause of the increasing deformation of the joint. According to the stress state of the plastic hinges, the elastoplastic rotational behavior of the connection can be deduced at any loading state. The analysis model of the plastic hinge lines for flanges of BE and CE at ultimate state is represented in Fig. 12.

The analysis model of the plastic hinge lines at the ultimate state indicate the damage mechanism of BE and CE, which is the main control factor for the elastoplastic rotational behavior of the connection. So the stress and deformation performance of the connection at elastoplastic stage can be obtained by the analysis model of plastic hinge lines. And the damage performance of the connection can be estimated by the analysis model.

The analysis results shown in Fig. 10. indicate that at stage O-I or close to state point I, the plastic hinge lines of BE and CE of specimens S+4, S+5 and SL1 form simultaneously, and the plastic hinge lines of CE of specimens S+1, S+3 form, and the plastic hinge lines of BE of specimens S+2, ST1, ST2 and SL2 form. And the large plastic deformation of BE of specimens S+4 and S+5 occurs, and the little plastic deformation of BE of specimens ST1, ST2, SL1 and SL2 occurs. In conclusion, when the plastic hinge lines of BE and CE form simultaneously, the plastic deformation of the joint increases rapidly. Plastic hinges 1 and 2 at BE and CE are shown in Fig. 13. Because the plastic deformation of plastic hinge 2 in the tension state is more than that in the compression state due to the blocking effect of the confined concrete. When plastic hinge 2 is in the tension state, there is a relative angle δ between plastic hinges 1 and 2. When the stress state of plastic hinge 2 changes from tension to compression, there is no significant change in the relative angle δ. The center of the M_j-θ_b hysteretic loops deviates from the coordinate origin, and

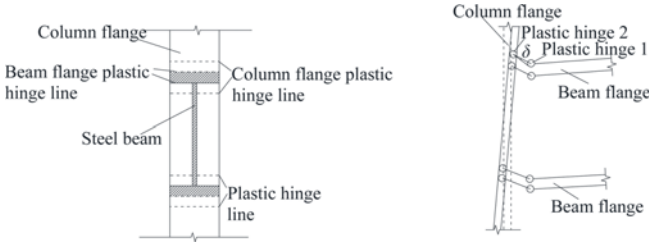

Fig. 13. Analysis Model of Simultaneous Yielding of Column and Beam Flange Plates

the direction of the deviating is that of θ_b corresponding to plastic hinge 2 in the tension state.

As shown in Fig. 7 for the specimens with β of 3 and 4, the shape of the M_j-θ_b hysteresis loops is in strong agreement with that of the M_j-θ_r hysteresis loops. Because the rotational deformation of BE rapidly increases with the increasing of the relative angle δ, θ_r of the connection is controlled by BE rotation θ_b. The shape of the M_j-θ_b and M_j-θ_c hysteresis loops differ greatly. Correspondingly, the centers of the M_j-θ_r and M_j-θ_b hysteretic loops deviate from the coordinate origin, and the deviation distance increases with the increasing of the loading loop cycles.

5. Effecting Factors on Performance of Moment-Rotation Envelope Curves

In order to analyze the influence of the design parameters on the rotational behavior of the connection and establish the analytical model of the moment-rotation envelope curves, the parametric analysis is presented for the moment-rotation envelope curves. Figs. 14, 15 and 16 demonstrate the effects of β, n and column section shape on the performance of moment-rotation envelope curves respectively. The curves of specimens S+1, S+2, S+3, ST1, ST2, SL1 and SL2 in Figs. 14, 15 and 16 are the envelopes of the M_j-θ_r hysteresis curves. In order to study the elastic bending rigidities of specimens S+4 and S+5, the curves of specimens S+4 and S+5 in Figs. 14, 15 and 16 are the envelopes of the M_j-θ_c hysteresis curves.

As shown in Fig. 14(a), with the increasing of β, the elastic bending rigidity of the S+ specimens under negative bending moment gradually increases. Under positive bending moment the elastic bending rigidity of specimen S+5 exceeds that of specimens S+4 and S+1, while the elastic bending rigidity of specimen S+4 is slightly less than that of specimen S+1. Based on the previous studies on the performance of CFST member under bending moment by Zhong (2003), the column section is divided into compression and tension areas. In the compression area both the steel tube and the confined concrete sustain compressive loading. In the tensile area, due to the confined concrete cracking only the steel tube sustains tension, and the confined concrete supports the steel tube. As the S+ cross section

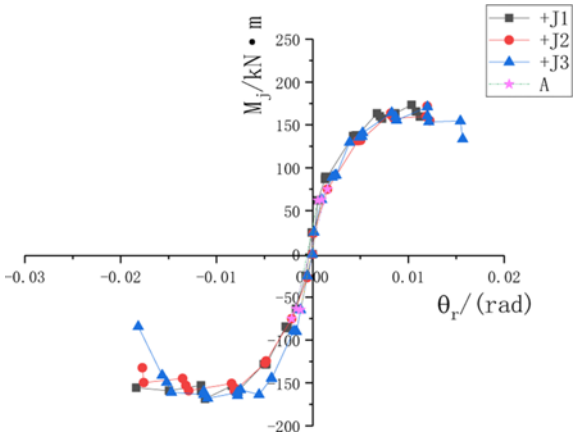

Fig. 15. Effect of n of Column on Performance of Moment-Rotation Envelope Curves

is symmetrical, the geometric characteristics of the steel tubes and the confined concrete in the compression area of S+ specimens are generally similar to those with the same β. So the shape of the envelopes of the S+ specimens in Fig. 14(a) under positive bending moment is almost equal to that under negative bending moment.

Under negative bending moment the geometric characteristic of the steel tubes and the confined concrete in the compression area of specimen ST1 is in strong agreement with that of specimen ST2. So the elastic bending rigidities of specimens ST1 and ST2 under negative bending moment in Fig. 14(b) are the same in the main. Under positive bending moment, the geometric characteristic of the steel tubes and the confined concrete in the compression area of specimen SL1 is in strong agreement with that of specimen SL2. So the elastic bending rigidities of specimens SL1 and SL2 under positive bending moment in Fig. 14(c) is the same in the main. As the ST and SL cross sections are asymmetric, changes in the bending moment direction alter the geometric characteristics of the steel tubes and the confined concrete in the compression area. The elastic bending rigidities of the ST specimens under positive bending moment are distinct to those under negative bending moment, and the elastic bending rigidities of the SL specimens under negative bending moment are distinct to those

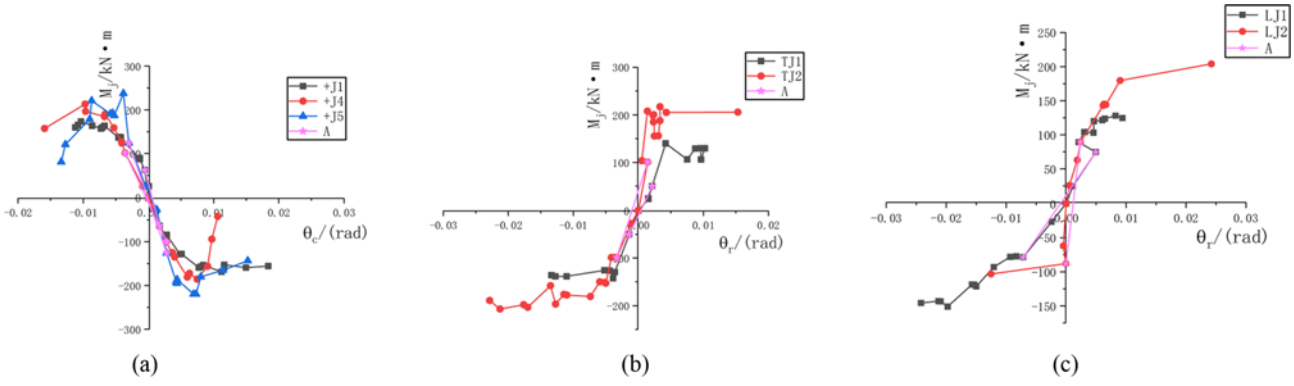

Fig. 14. Effect of β on Performance of Moment-Rotation Envelope Curves: (a) S+ Specimens, (b) ST Specimens, (c) SL Specimens

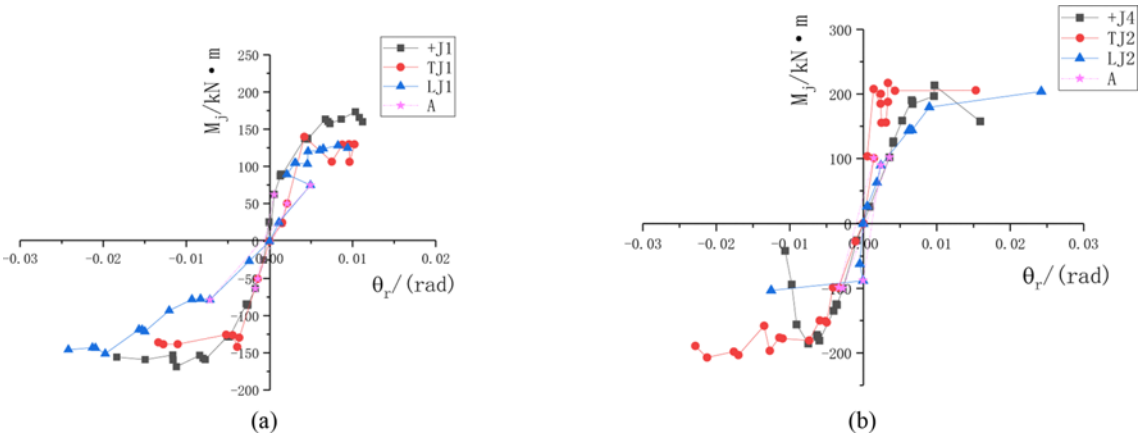

Fig. 16. Effect of the Column Section Shape on Performance of Moment-Rotation Envelope Curves: (a) Specimens with β of 2 (b) Specimens with β of 3

under positive bending moment.

As demonstrated in Fig. 15, under positive bending moment the elastic bending rigidities of specimens S+1, S+2 and S+3 are almost identical. Under negative bending moment, the elastic bending rigidities of specimens S+1, S+2 and S+3 exhibit a slight increase with the increasing of n. Thus, n has an insignificant effect on the elastic bending rigidity.

The elastic bending rigidity of specimen SL1 is significantly lower than that of specimens S+1 and ST1 as shown in Fig. 16(a). Because under negative bending moment, the torque redistributes the stress of the limbs parallel and vertical to the beams of specimen SL1. As shown in Fig. 16, under negative loading the elastic bending rigidities of specimens S+1 and S+4 are in strong agreement with those of specimens ST1 and ST2, respectively. It is indicated that the geometric characteristics of the steel tubes and the confined concrete in the compression area of specimens S+1 and S+4 under negative bending moment are close to those of specimens ST1 and ST2, respectively.

Figures 16(a) and 16(b) reveals that under positive loading the elastic bending rigidity of specimen S+1 (ST2) is noticeably higher than that of specimens ST1 and SL1 (S+4 and SL2). The results indicate that under positive loading, with the increasing of β the flexural behavior of the S+ specimen weakens, and the flexural behavior of the ST specimen improves.

6. Calculation of Elastic Bending Rigidity of Joint

6.1 Analysis Model for Unified Material of Joint

The steel tubes of the limbs parallel and vertical to the beams are connected by welding to form an entity. Based on unified design theory under bending moment by Zhong (2006), the confined concrete in the compressive region is restrained by the tightening force of the steel tubes. Thus, the steel tubes and the confined concrete in the compressive region can be analyzed as an unified material. Based on existing research by Mander et al. (1988), the confinement force of the confined concrete is typically produced at the corner of the steel tube, and the external contour line of the effective constrained region of the confined concrete is a para-curve along the diagonal of the steel tube. The effective constrained regions of the confined concrete are depicted as the shaded areas in Fig. 17 when the neutral axis moves between lines m and e (r and s).

When the neutral axis moves between m-e, the analysis model of the tightening-ring force for S+ specimens is shown in Fig. 18.

In Fig. 18 p_{hw} and p_{vw} are the horizontal and the vertical constraint reaction stresses on the steel tube exerted by the confined concrete in the limb parallel to the beam respectively, and p_{hf} and p_{vf} are the horizontal and the vertical constraint reaction stresses on the steel tubes exerted by the confined concrete in the limbs vertical to the beam respectively. And σ_{sw} and σ_{sf} are the transverse tension stresses of the steel webs of the limbs parallel and vertical to the beams respectively, b_w and b_f are the vertical lengths of the confined concrete of the limbs parallel and vertical to the beams respectively, a_{wn1} and a_{fn1} are the lengths of the steel webs of the limbs parallel and vertical to the beams respectively on the left side of the neutral axis u. Considering that the boundary shapes of the steel tubes of the limbs parallel and vertical to the beams are square or nearly square, and the influence of the constraint reaction stresses on the whole mechanical property and the damage performance of MCFST member, it is assumed that the boundary shapes of the steel tubes of the limbs parallel and vertical to the beams are square and the constraint reaction stresses exerted by the confined concrete is uniformly distributed. The assumption is used to analyze the mechanical equilibrium condition of the constraint reaction stresses on the steel tubes, and not local stress concentration, and mechanical and damage characteristics of the steel tubes induced by local buckling. According to the unified design theory and the mechanical equilibrium, the following equation is derived:

$$p_{hw} = p_{vw} = p_{hf} = p_{vf} = p. \tag{5}$$

According to the mechanical equilibrium condition of the constraint reaction stresses on the steel tubes, the mechanical equilibrium equations can be obtained by the following formula:

$$p\left[b_w a_{wn1} - S_1 - 2S_2 + 2b_f a_{fn1} - 2S_3 - 2S_4\right] = 2\sigma_{sw} t_{w1} a_{wn1} + 2\sigma_{sf} t_{w2} a_{fn1}. \tag{6}$$

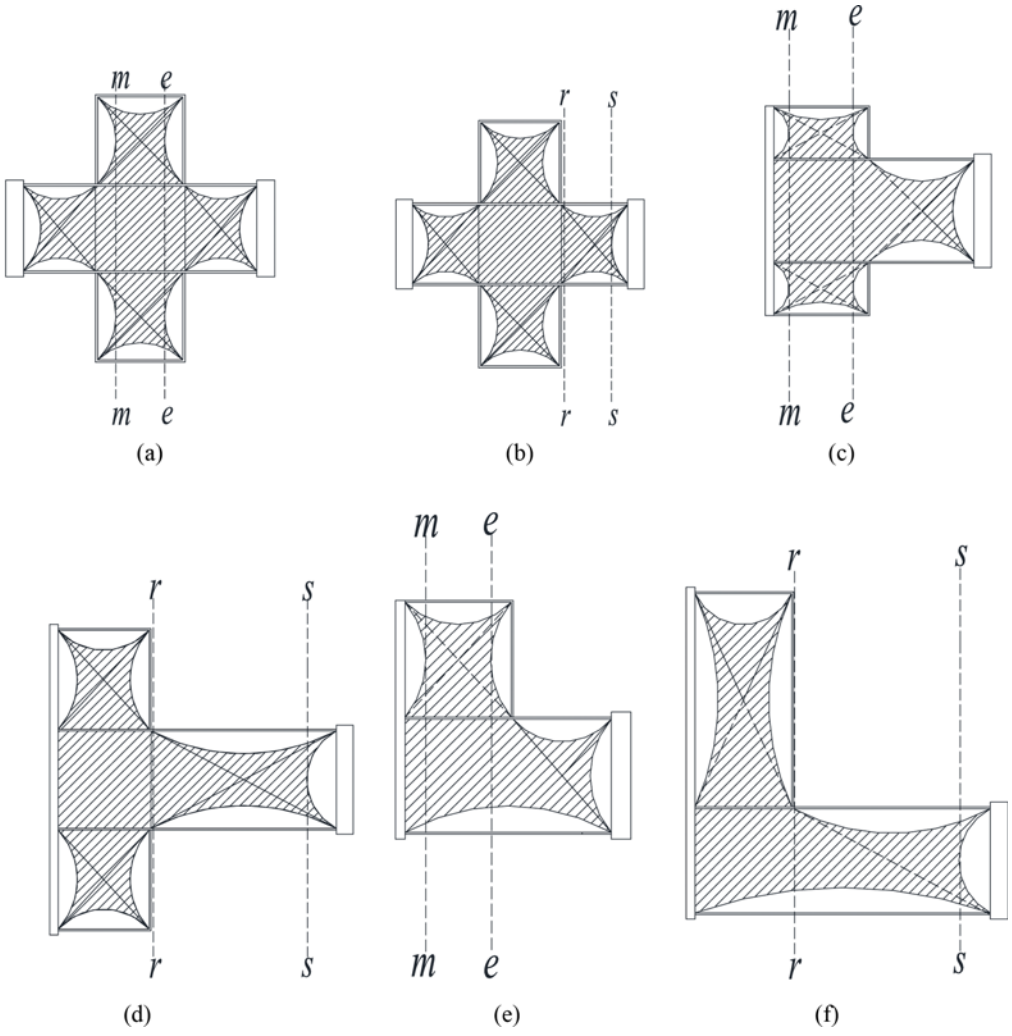

Fig. 17. Movement Range of Neutral Axis: (a) Range *m*-*e* for S+ Specimens, (b) Range *r*-*s* for S+ Specimens, (c) Range *m*-*e* for ST Specimens, (d) Range *r*-*s* for ST Specimens, (e) Range *m*-*e* for SL Specimens, (f) Range *r*-*s* for SL Specimens

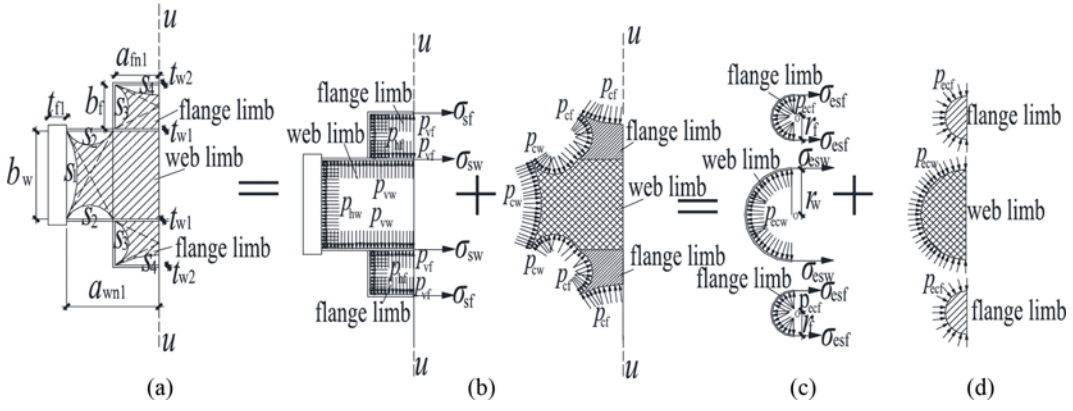

Fig. 18. Analysis Model of Tightening-Ring force in Compressive Region on left of *u* for S+ Specimens: (a) Compressive Region on Left of *u*, (b) Steel Tubes, (c) Effective Confined Concrete, (d) Equivalent Steel Tube and Confined Concrete

Therefore, the constraint reaction stresses on the steel tubes of the limbs parallel and vertical to the beams p are given as follows:

$$p = \frac{2\sigma_{sw} t_{w1} a_{wn1} + 2\sigma_{sf} t_{w2} a_{fn1}}{\left[b_w a_{wn1} - S_1 - 2S_2 + 2b_f a_{fn1} - 2S_3 - 2S_4\right]}. \quad (7)$$

As shown in Fig. 18, the tightening-ring stresses p_{cw} and p_{cf} of the confined concrete in the effective constrained region of the limbs parallel and vertical to the beams have a nonuniform distribution, and the boundary condition of the confined concrete is complex. Thus, analysis of the tightening-ring stresses proves

to be a challenge. For convenience, according to the analysis thought conducted by Zhong (2006) which the behaviors of various forms of members are obtained by use of equivalent circular members including solid and hollow cross sections, a differential element of the unified material is introduced, considering the contribution of the effective constrained regions of the confined concrete to the whole mechanical property of MCFST member. The analysis model of the unified material is consisted by the differential element, and follows the basic assumptions:1) a basic composition unit of the unified material is a differential element which is the differentiation result of the whole mechanical property and damage performance of MCFST member, and not a differential element which has mechanical property of concrete and steel material; 2) the tightening-ring stresses of the basic composition units of the unified material are effective; 3) the tightening-ring stresses of the basic composition units are uniformly; 4) the boundary of the basic composition unit is circular. The model of the unified material is used to analyze the whole mechanical property and damage performance of MCFST member, and not local mechanical and damage characteristics of MCFST member, steel tube buckling, the cracks and damage of the confined concrete.

According to the aforementioned experimental results and the unified design theory, the steel webs of the limb parallel to the beam are the first to yield, which indicates the unified material gets into elastoplastic stage. And the failure features of the steel webs are the first to appear, which indicates the unified material gets into failure stage. The elastoplastic and damage performances of the unified material of the joint are controlled by the stress state and failure pattern of the steel webs of the limb parallel to the beam. So the material properties and thickness of the steel tube of the differential element are the same with those of the steel webs of the limb parallel to the beam. Based on the above assumption, the confined concrete of the differential element is obtained from the effective constraint regions as shown in Fig. 18(a). According to the equilibrium conditions of the tightening-ring stresses of the confined concrete, the following equation can be obtained.

$$p_{ecw} = p_{ecf} = p_e \tag{8}$$

$$p(b_w a_w + 2b_f a_f) = 2\sigma_{sw} t_{w1} a_{wn1} + 2\sigma_{sf} t_{w2} a_{fn1} \tag{9}$$

$$p(b_w a_w + 2b_f a_f) = 2\int_0^{\pi} \frac{p_e r_1^2 \sin\phi}{2} d\phi + 4\int_0^{\pi} \frac{p_e r_2^2 \sin\phi}{2} d\phi = \frac{2p_e[b_w a_{wn1} - S_1 - 2S_2]}{\pi} + \frac{4p_e[b_f a_{fn1} - S_3 - S_4]}{\pi} \tag{10}$$

Where p_{ecw} and p_{ecf} are the equivalent tightening-ring stresses of the confined concrete in the effective constrained regions of the limbs parallel and vertical to the beams in the model of equivalent concrete-filled circular steel tubular, $d\phi$ is the differential element in the model of equivalent concrete-filled circular steel tubular. The equivalent tightening-ring stresses p_e of the confined concrete in the model of equivalent concrete-filled circular steel tube is obtained by the following formula:

$$p_e = \frac{\pi(2\sigma_{sw} t_{w1} a_{wn1} + 2\sigma_{sf} t_{w2} a_{fn1})}{2([b_w a_{wn1} - S_1 - 2S_2] + 2[b_f a_{fn1} - S_3 - S_4])}, \tag{11}$$

where α_1 is the ratio of the steel content of the limb parallel to the beam. According to the definition of the confinement coefficient by Zhong (2003), the confinement coefficient ξ_w of the limb parallel to the beam can be obtained by the following formulas:

$$\xi_w = \alpha_1 f_y / f_c = \frac{2p_e}{f_c} = \frac{\pi(2\sigma_{sw} t_{w1} a_{wn1} + 2\sigma_{sf} t_{w2} a_{fn1})}{f_c([b_w a_{wn1} - S_1 - 2S_2] + 2[b_f a_{fn1} - S_3 - S_4])}. \tag{12}$$

And the confinement coefficient ξ_f of the limbs vertical to the beam can be obtained by the following formulas:

$$\xi_f = \alpha_2 f_y / f_c = \frac{2p_e f_y}{\sigma_{sf} f_c} = \frac{f_y \pi(2\sigma_{sw} t_{w1} a_{wn1} + 2\sigma_{sf} t_{w2} a_{fn1})}{\sigma_{sf} f_c([b_w a_{wn1} - S_1 - 2S_2] + 2[b_f a_{fn1} - S_3 - S_4])}, \tag{13}$$

where α_2 is the ratio of the steel content of the limbs vertical to the beam. The confinement coefficient ξ of the whole unified material in the compressive region on left and right of u for S+ specimens can be obtained by the following formula:

$$\xi = \frac{\xi_w A_{c1} + \xi_f A_{c2}}{A_{c1} + A_{c2}} = \frac{\left\{\frac{\pi}{f_c}(b_w a_{wn1} - S_1 - 2S_2) + \frac{2f_y \pi}{\sigma_{sf} f_c}[b_f a_{fn1} - S_3 - S_4]\right\}(2\sigma_{sw} t_{w1} a_{wn1} + 2\sigma_{sf} t_{w2} a_{fn1})}{([b_w a_{wn1} - S_1 - 2S_2] + 2[b_f a_{fn1} - S_3 - S_4])^2}, \tag{14}$$

where A_{c1} and A_{c2} are the total areas of the confined concrete in the effective constrained region of the limbs parallel and vertical to the beams respectively. When the neutral axis moves between *m*-*e*, the analysis model of the tightening ring force for ST specimens is shown in Figs. 19 and 20.

Similarly, according to the above methods, the confinement coefficient ξ of the whole unified material in compressive region on left and right of u for ST specimens is obtained by the following formulas:

$$\xi = \frac{(A_{s1} + A_{s2}) f_y}{(A_{c1} + A_{c2}) f_c} = \frac{\xi_w A_{c1} + \xi_f A_{c2}}{A_{c1} + A_{c2}} = \frac{\left\{\frac{\pi}{f_c} b_w a_{wn1} + \frac{2f_y \pi}{\sigma_{sf} f_c}[b_f a_{fn1} - S_3 - S_4]\right\}(2\sigma_{sw} t_{w1} a_{wn1} + 2\sigma_{sf} t_{w2} a_{fn1})}{(b_w a_{wn1} + 2[b_f a_{fn1} - S_3 - S_4])^2}, \tag{15}$$

$$\xi = \frac{(A_{s1} + A_{s2}) f_y}{(A_{c1} + A_{c2}) f_c} = \frac{\xi_w A_{c1} + \xi_f A_{c2}}{A_{c1} + A_{c2}} = \frac{\left\{\frac{\pi}{f_c}(b_w a_{wn1} - S_1 - 2S_2) + \frac{2f_y \pi}{\sigma_{sf} f_c}([b_f a_{fn1} - S_3 - S_5]\right\}(2\sigma_{sw} t_{w1} a_{wn1} + 2\sigma_{sf} t_{w2} a_{fn1})}{([b_w a_{wn1} - S_1 - 2S_2] + 2[b_f a_{fn1} - S_3 - S_5])^2}, \tag{16}$$

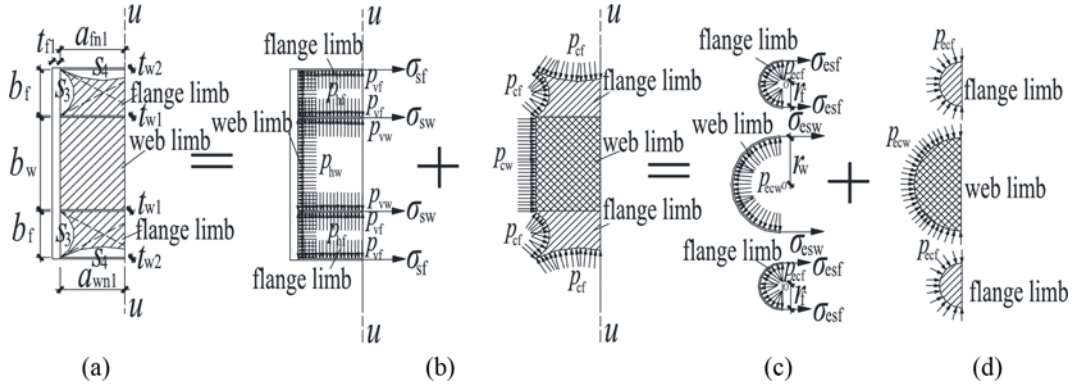

Fig. 19. Analysis Model of Tightening-Ring Force in Compressive Region on Left of *u* for ST Specimens: (a) Compressive Region on Left of *u*, (b) Steel Tubes, (c) Effective Confined Concrete, (d) Equivalent Steel Tube and Confined Concrete

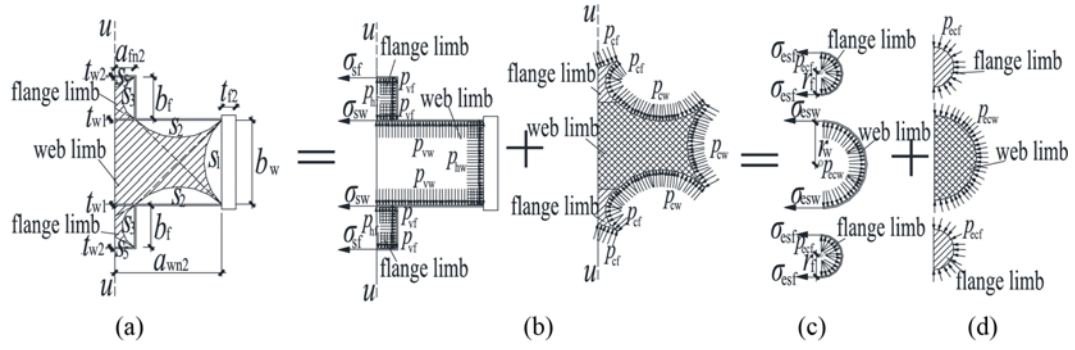

Fig. 20. Analysis Model of Tightening-Ring Force in Compressive Region on Right of *u* for ST Specimens: (a) Compressive Region on Right of *u*, (b) Steel Tubes, (c) Effective Confined Concrete, (d) Equivalent Steel Tube and Confined Concrete

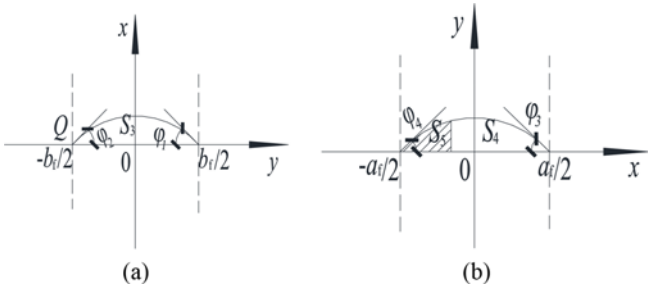

Fig. 21. Local Coordinate System for the Regional Boundary of Effective Restraint Area of the Confined Concrete: (a) Local Coordinate System for S_3, (b) Local Coordinate System for S_4 and S_5

where A_{s1} and A_{s2} are the total areas of the limbs parallel and vertical to the beams respectively in the model of equivalent concrete-filled circular steel tubular, a_{wn2} and a_{fn2} are the length of the steel webs of the limbs parallel and vertical to the beams respectively on the right side of the neutral axis *u*. The external contour line of the shaded area S_3 is demonstrated in the following local coordinate system as shown in Fig. 21.

In Fig. 21(a), the intersection point between the starting point of the para-curve corresponding to the limb parallel to the beam and the *y*-axis is point $Q(-b_f/2, 0)$. The slope of the para-curve at the intersection point is given as:

$$tg\varphi_2 = \frac{b_f/2}{a_f/2} = \frac{b_f}{a_f}, \tag{17}$$

where a_f is the length of the confined concrete of the limbs vertical to the beam in web direction. The function expression of the para-curve is described as:

$$y = -\frac{b_f}{a_f^2}\left(x - \frac{a_f}{2}\right)\left(x + \frac{a_f}{2}\right), \tag{18}$$

The areas of the planar figure surrounded by the external contour lines of S_3, S_4 and S_5 in Fig. 21 are obtained as:

$$S_3 = \frac{b_f}{4} \times \frac{a_f}{2} \times \frac{4}{3} = \frac{a_f b_f}{6}. \tag{19}$$

$$S_5 = \frac{a_{fn2}}{4} \times \frac{b_f}{2} \times \frac{4}{3} = \frac{a_{fn2} b_f}{6}, \tag{20}$$

$$S_4 = \frac{1}{2} \times \frac{a_f}{4} \times \frac{b_f}{2} \times \frac{4}{3} = \frac{a_f b_f}{12}. \tag{21}$$

Similarly, the areas of the planar figure surrounded by the external contour lines of S_1, S_2, S_6 and S_7 are given as:

$$S_1 = \frac{b_w}{4} \times \frac{(a_{wn1} - a_{fn1})}{2} \times \frac{4}{3} = \frac{b_w (a_{wn1} - a_{fn1})}{6}, \tag{22}$$

$$S_2 = \frac{(a_{wn1} - a_{fn1})}{4} \times \frac{b_w}{2} \times \frac{4}{3} = \frac{b_w (a_{wn1} - a_{fn1})}{6}, \tag{23}$$

$$S_6 = \frac{a_{wn1}}{4} \times \frac{b_w}{2} \times \frac{4}{3} = \frac{a_{wn1} b_w}{6}, \tag{24}$$

$$S_7 = \frac{b_w\left(a_w - a_{wn1}\right)}{6}. \tag{25}$$

When the neutral axis moves between *m*-*e*, the analysis model of the tightening-ring force for SL specimens is shown in Figs. 22 and 23.

And the confinement coefficient ξ of the whole unified material in compressive region on left and right of *u* for SL specimens is obtained by the following formulas:

$$\xi = \frac{\xi_w A_{c1} + \xi_f A_{c2}}{A_{c1} + A_{c2}} = \frac{\left\{\frac{\pi}{f_c}(b_w a_{wn1} - S_6) + \frac{f_y \pi}{\sigma_{sf} f_c}[b_f a_{fn1} - S_3 - S_4]\right\}(2\sigma_{sw} t_{w1} a_{wn1} + 2\sigma_{sf} t_{w2} a_{fn1})}{([b_w a_{wn1} - S_6] + [b_f a_{fn1} - S_3 - S_4])^2}, \tag{26}$$

$$\xi = \frac{\xi_w A_{c1} + \xi_f A_{c2}}{A_{c1} + A_{c2}} = \frac{\left\{\frac{\pi}{f_c}(b_w a_{wn1} - S_1 - S_2 - S_7) + \frac{f_y \pi}{\sigma_{sf} f_c}([b_f a_{fn1} - S_3 - S_5]\right\}(2\sigma_{sw} t_{w1} a_{wn1} + 2\sigma_{sf} t_{w2} a_{fn1})}{([b_w a_{wn1} - S_1 - S_2 - S_7] + [b_f a_{fn1} - S_3 - S_5])^2}. \tag{27}$$

When the neutral axis moves between *r* and *s*, the compressive region for S+ specimens, ST specimens and SL specimens can be obtained by the analysis model shown as in Figs. 24, 25 and 26 respectively.

Similarly, according to the location of the neutral axis *u*, a_{fn1}, a_{fn2}, a_{wn1} and a_{wn2} can be determined. And the areas S_1-S_6 can be calculated by the external contour lines of the ineffective constrained regions of the confined concrete. The results reveal minimal variations in confinement coefficient ξ when the neutral axis moves between *m*-*e* and *r*-*s*. In order to simplify the calculation, it is assumed that ξ is established when the neutral axis is in the centroid of the column section. According to the above basic assumptions of the differential element of the unified material, the composition methods and the performance features of the differential element are the same with those of the unified material of circular CFST members. So according to the composite characteristics indexes of circular CFST members by Zhong (2003), the composite characteristics indexes of the differential element are obtained, and the elastic modulus E_{sc} of the unified material composed of the special-shaped steel tubulars and the confined concrete in the compressive region for event O-I is given as:

$$E_{sc} = \left(0.192\frac{f_y}{235} + 0.488\right)(1.212 + D\xi + F\xi^2) f_{ck} E_s / (0.67 f_y), \tag{28}$$

where $D = 0.1759\frac{f_y}{235} + 0.974$, $F = -0.1038\frac{f_{ck}}{20} + 0.0309$. From the equation above, it can be seen that E_{sc} is obtained by the confinement

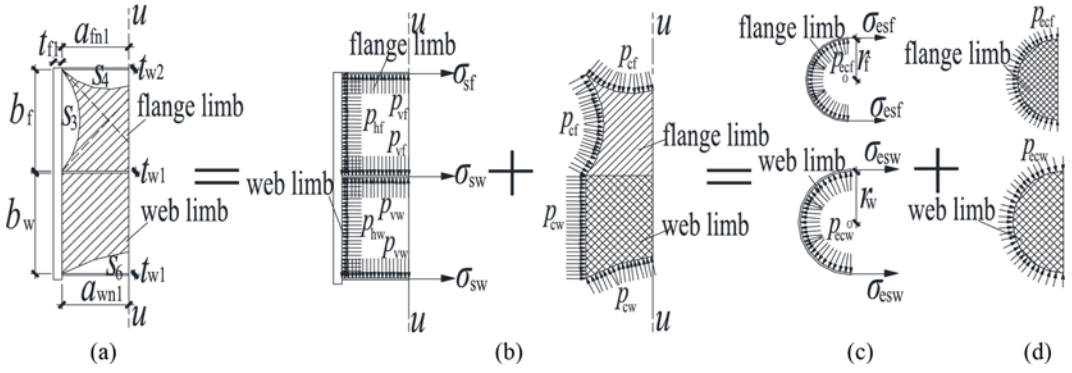

Fig. 22. Analysis Model of Tightening-Ring Force in Compressive Region on Left of *u* for SL Specimens: (a) Compressive Region on Left of *u*, (b) Steel Tubes, (c) Effective Confined Concrete, (d) Equivalent Steel Tube and Confined Concrete

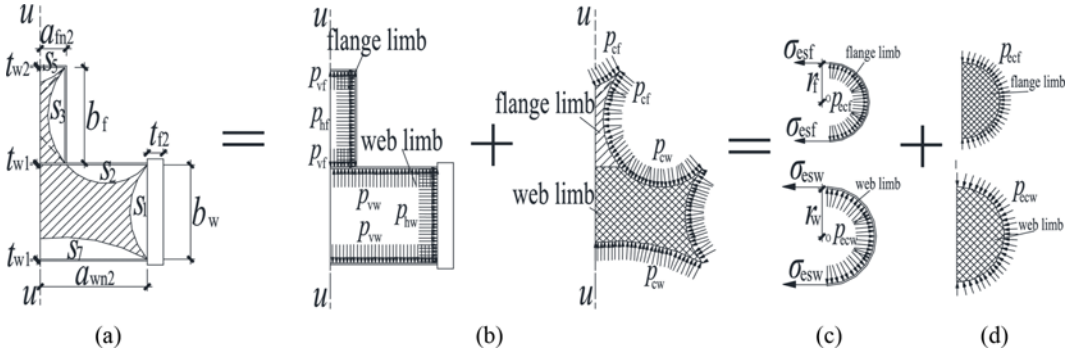

Fig. 23. Analysis Model of Tightening-Ring force in Compressive Region on Right of *u* for SL Specimens: (a) Compressive Region on Right of *u*, (b) Steel Tubes, (c) Effective Confined Concrete, (d) Equivalent Steel Tube and Confined Concrete

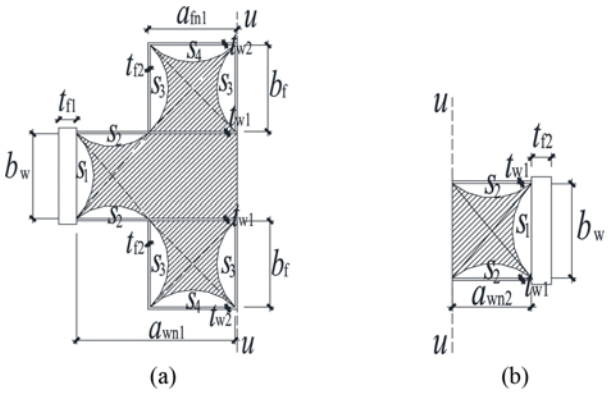

Fig. 24. Effective Constrained Region for S+ Specimens: (a) Compressive Region on Left of *u*, (b) Compressive Region on Right of *u*

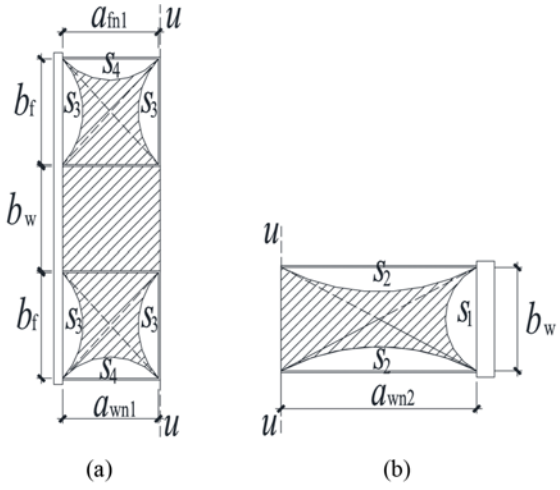

Fig. 25. Effective Constrained Region for ST Specimens: (a) Compressive Region on Left of *u*, (b) Compressive Region on Right of *u*

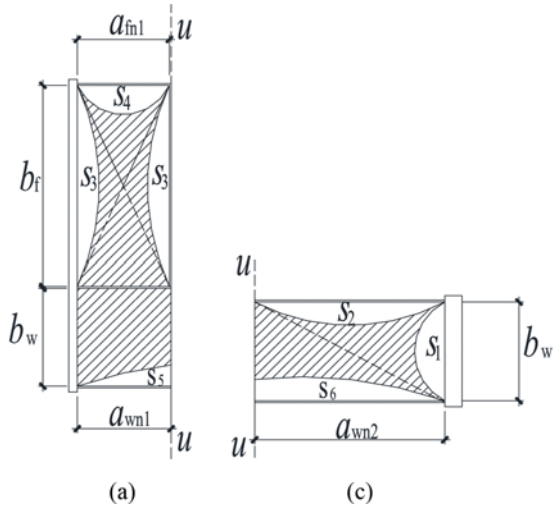

Fig. 26. Effective Constrained Region for SL Specimens: (a) Compressive Region on Left of *u*, (b) Compressive Bending Region on Right of *u*

coefficient of the whole unified material and the design parameters of the specimens.

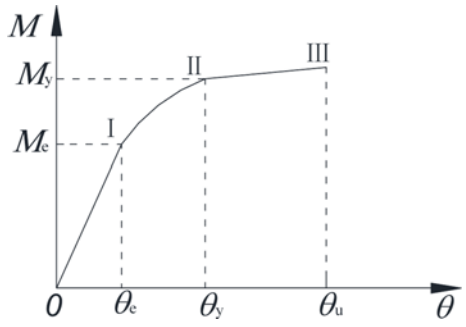

Fig. 27. Analysis Model of Moment-Rotation Relationship

6.2 Performance-Based Calculation for Elastic Bending Rigidity of Joint

Based on the analysis results in Fig. 7, the analysis model of the bending moment-rotation relationship for the joint is shown in Fig. 27, where I is the starting point for the elastoplastic stage of the steel webs of the limb parallel to the beam, II and III are the yield and the limit points of the specimens respectively, M_e and M_y are the bending moments at state points I and II respectively, and θ_e, θ_y and θ_u are the relative rotations at state points I, II and III respectively.

According to the elastic moment resisting modulus of circular CFST flexural members proposed by Zhong (2006), the elastic moment resisting modulus E_{scm} of the joint at event I can be obtained by the elastic modulus E_{sc} of the unified material in the compressive region for events O-I as follows:

$$E_{scm} = \frac{(1+\gamma\alpha_E)}{(1+\lambda\alpha_E)} \cdot \frac{(1+\lambda)}{(1+\gamma)} E_{sc} . \tag{29}$$

where $\alpha_E = \frac{E_s}{E_c}$, $\gamma = \frac{I_s}{I_c}$, $\lambda = \frac{A_s}{A_c}$, A_s and I_s are the cross section area and the moment of inertia of the special shaped steel tube respectively, A_c and I_c are the cross section area and the moment of inertia of the confined concrete respectively.

According to the composite moment of inertia I_{sc0} for circular CFST flexural members proposed by Zhong (2006), the composite moment of inertia I_{sc0} for the joint is obtained as follows:

$$I_{sc0} = I_s + I_c . \tag{30}$$

Due to the concrete cracking the confined concrete in tensile area is invalid, which consequently weakens the elastic bending rigidity of the joint. Based on the calculation of the modified composite moment of inertia of circular CFST flexural members considering weakening effects of the concrete cracking proposed by Zhong (2006), the modified composite moment of inertia I_{sc} for the joint is given as:

$$I_{sc} = (0.6625 + 0.9375\alpha) I_{sc0} . \tag{31}$$

According to the experimental results, β and the cross-section shape have an obvious influence on the elastic bending rigidity of the joint. $f(\beta)$ is defined as the influence coefficient of β on the elastic bending rigidity K_e of the joint. Based on the analysis model of the bending moment-rotation relationship for circular CFST

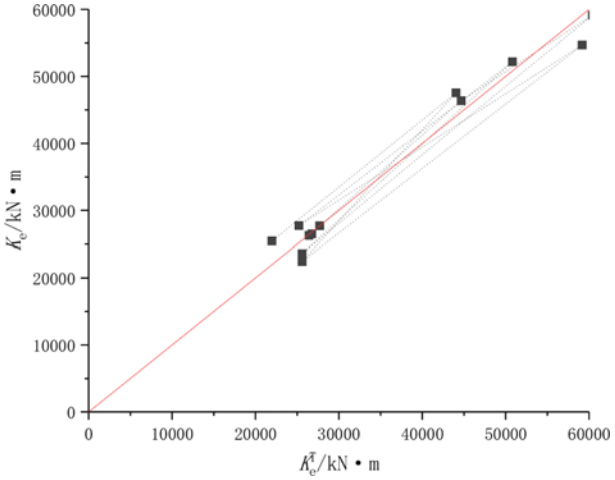

Fig. 28. omparison of Theoretical and Experimental Results of Elastic Bending Rigidity of Joint

flexural members proposed by Zhong (2006), the calculation method of the elastic bending rigidity of the joint can be given by:

$$K_e = f(\beta)(0.6625+0.9375\alpha)E_{scm}I_{sc0} = f(\beta)\frac{(1+\gamma\alpha_E)}{(1+\lambda\alpha_E)}\cdot\frac{(1+\lambda)}{(1+\gamma)}(0.6625+0.9375\alpha)E_{sc}I_{sc0}. \quad (32)$$

Through the regression analysis of the experimental results of S+ specimens, the mathematical expression for $f(\beta)$ is given as follows:

$$f(\beta) = -0.1561\beta + 1.5596. \quad (33)$$

Through the regression analysis of the experimental results of ST and SL specimens, the mathematical expression for $f(\beta)$ is obtained as follows:

$$f(\beta) = -0.0591\beta + 1.1569. \quad (34)$$

Figure 28 shows the comparison of the theoretical elastic bending rigidity K_e of the joint and the experimental elastic bending rigidity K_e^T. In Fig. 28 the average value of the error percentage of the theoretical elastic bending rigidity K_e is 4.34%, it is seen that the theoretical results correlate well with the experimental data.

7. Analytic Model of M_j-θ_r Curve Of Joint

The analytic expression of the M_j-θ_r curves of the ring board CFST connection proposed by Han et al. (2009) is given as following:

$$M_j = n_s \cdot M_{uj} \cdot In\left(1+\frac{\theta_r}{n_s\cdot\theta_0}\right), \quad (35)$$

where M_{uj} is the ultimate bending moment of the ring board CFST connection, θ_e is the reference rotation and is obtained as follows :

$$\theta_0 = \frac{M_{uj}}{K_e}. \quad (36)$$

n_s is the parameter related to the shape of the M_j-θ_r curves, and is obtained as follows :

$$0.2 \le n_s = 0.12\cdot In(\theta_0)+1.27 \le 0.36, \quad (37)$$

when $n_s > 0.36$, the value n_s is 0.36.

Based on the previous study results, the bending failure of MCFST connection is in accordance with the yielding line damage mechanism, and the distortion of the plastic hinges exerts a great influence on the deformation of the joint. The damage mechanism of MCFST connection is the same with that of the ring board CFST connection. So the analytic expression of the M_j-θ_r curve of the ring board CFST connection is used for that of MCSFT connection. However, these parameters in the moment-rotation analytic expression are determined by fitting experimental results. In other words, it is imperative to propose a practical and accurate moment-rotation relation model for MCSFT connections baesed on the experiment results. In order to account for the influence of the design parameters and yielding lines damage mechanism on the shape of the M_j-θ_r curves of MCSFT connections. k is defined as the influence parameter of the cross-section shape and β. The M_j-θ_r curves of MCSFT connections can be analytically expressed as:

$$M_j = n_s \cdot M_{uj} \cdot In\left[k\left(1+\frac{\theta_r}{n_s\cdot\theta_0}\right)\right]. \quad (38)$$

By fitting analysis of the experimental results, k of S+ specimens can be expressed in the following formula:

$$k = -1.2538\beta + 4.9461. \quad (39)$$

k of ST and SL specimens can be expressed in the following formula:

$$k = 0.2898\beta + 1.431. \quad (40)$$

Comparison of the theoretical and experimental results of the M_j-θ_r curves is represented in Fig. 29. In the analysis, in order to obtain M_j-θ_r continuous curves the direction of part rotational displacement points of the specimens is adjusted to suit continuity of the curves.

The results reveal that the theoretical calculations of specimens S+1, S+2, S+3, ST1, ST2, SL1 and SL2 are in good agreement with the experimental results. However, a discrepancy is observed between the two result sets for specimens S+4 and S+5 under negative bending moment. The results show that the simultaneous yielding of the column and beam flange plates has more and more effect on the elastoplastic rotational behavior of the connection with the increasing of β. So the influence of simultaneous yielding should be considered on the analytic expression of the M_j-θ_r curve of the specimens with β of 4.

8. Conclusions

In this study, based on the research findings the following conclusions are determined as follows:

1. At stage O-I, M_j-θ_c, M_j-θ_b and M_j-θ_r hysteretic curves for specimens S+1, S+2, S+3 and SL1 generally exhibit a linear relationship. M_j-θ_c hysteretic curves of specimens S+4, S+5,

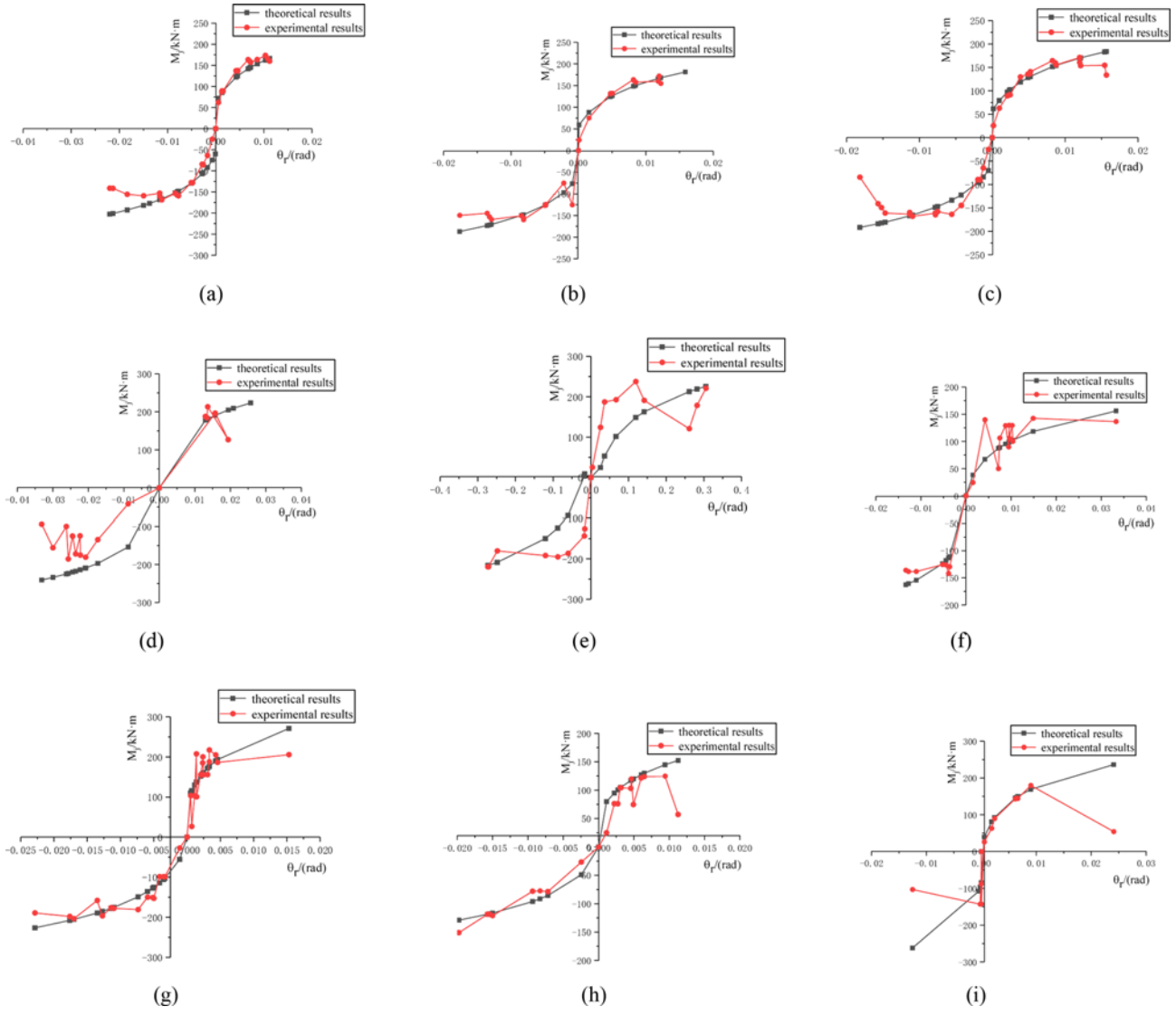

Fig. 29. Comparison of Theoretical and Experimental Results of M_j-θ_r Curves: (a) S+1, (b) S+2, (c) S+3, (d) S+4, (e) S+5, (f) ST1, (g) ST2, (h) SL1, (i) SL2

ST1, ST2, and SL2 also follow a linear relationship. The large slipping of rotations θ_b of specimens S+4 and S+5 is observed, and the small slipping of rotations θ_b of specimens ST1, ST2, SL1 and *S*L2 is also observed. The shape of the M_j-θ_c hysteretic loops curves of the specimens S+1, S+2, S+3, ST1 and SL1 is similar to the M_j-θ_r hysteretic curves of those. At stage II-III the shape of the envelope of the M_j-θ_b hysteretic curves of specimen S+1 is close to that at stage O-I. After state point II, the plastic deformation of θ_r of specimen S+3 continuously increases with the increase of θ_b and θ_c.

2. When the stresses calculated by the strains in R1, R2, R3, R4, R5, R6, R7 and R8 begin to yield and exceed the yield point, it is indicated that the plastic hinges start to form and develops fully respectively. The produce orders of the plastic hinges vary with the design parameters of the specimens. The plastic hinges bear the load on the joint, and the deformation of the plastic hinges is produced, which is the main cause of the increasing deformation of the joint. The stress and deformation performance of the connection at elastoplastic stage can be obtained by the analysis model of plastic hinge lines. When the plastic hinge is in the tension state, there is a relative angle between the plastic hinges. When the stress state of the plastic hinge changes from tension to compression, there is no significant change in the relative angle.
3. With the increasing of β, the elastic bending rigidity of the S+ specimens under negative bending moment gradually increases. As the S+ cross section is symmetrical, the geometric characteristics of the steel tubes and the confined concrete in the compression area of S+ specimens are generally similar to those with the same β. The elastic bending rigidities of specimens ST1 and ST2 under negative bending moment are the same in the main, and the elastic bending rigidities

of specimens SL1 and SL2 under positive bending moment is the same in the main. n has an insignificant effect on the elastic bending rigidity. The elastic bending rigidity of specimen SL1 is significantly lower than that of specimens S+1 and ST1. Under negative loading the elastic bending rigidities of specimens S+1 and S+4 are in strong agreement with those of specimens ST1 and ST2, respectively.

4. Based on unified design theory under bending moment and the experimental results, performance-based calculation for the elastic bending rigidity of the joint is carried out following these steps: first, it is assumed that the constraint reaction stresses on the steel tubes is uniformly distributed, and according to mechanical equilibrium the constraint reaction stresses on the steel tubes of the limbs parallel and vertical to the beams is derived; secondly, a differential element of the unified material considering the contribution of the effective constrained regions of the confined concrete to the whole mechanical property of MCFST member is introduced, and the analysis model of the tightening-ring stresses in compressive region of the joint consisted by the differential elements is derived, and the confinement coefficient of the whole unified material in the compressive region can be obtained; thirdly, the elastic modulus of the unified material, and the elastic moment resisting modulus and the modified composite moment of inertia for the joint are given based on the calculation of the mechanical performance indexes of CFST flexural members; finally, through the regression analysis of the experimental results, the mathematical relationship between the elastic bending rigidity and β is obtained, and the elastic bending rigidity of the joint is derived.
5. Based on the yielding line mechanism and the analytic expression of the M_j-θ_r curves of the ring board CFST connection, the analytic expression of the M_j-θ_r curve of the MCFST connection is determined by fitting analysis of the experimental results. The theoretical results of specimens S+1, S+2, S+3, ST1, ST2, SL1 and SL2 are in good agreement with the experimental results. The influence of simultaneous yielding should be considered on the analytic expression of the M_j-θ_r curve of the specimens with β of 4.

Acknowledgments

This work is supported by the National Natural Science Foundation of China (Grant No.: 51808195), and the National Natural Science Foundation of China (Grant No.: 50978217). The financial support is highly appreciated.

Nomenclature

The following symbols are used in this paper:

A_c, A_s (mm^2) = Sectional areas of confined concrete and steel tube
A_{c1}, A_{c2} (mm^2) = Total areas of confined concrete in effective constraint region of limbs parallel and vertical to beams
a_f (mm) = Length of confined concrete of limbs vertical to beam in web direction
A_{s1}, A_{s2} (mm^2) = Total areas of limbs parallel and vertical to beams in model of equivalent concrete-filled circular steel tube
a_{wn1}, a_{fn1} (mm) = Lengths of steel webs of limbs parallel and vertical to beams on left side of neutral axis u
a_{wn2}, a_{fn2} (mm) = Length of steel webs of limbs parallel and vertical to beams on right side of neutral axis u
b_w, b_f (mm) = Vertical lengths of confined concrete of limbs parallel and vertical to beams
D, F = Calculation parameters for elastic modulus of unified material composed of special-shaped steel tubulars and confined concrete in compressive region
$d\phi$ = Differential element in model of equivalent concrete-filled circular steel tubular
E_c, E_s (MPa) = Elastic moduli of confined concrete and steel tube
$E_s^{'}$, $E_s^{''}$ (MPa) = Second and third modulus of steel material
E_{sc} (MPa) = Elastic modulus of unified material composed of special-shaped steel tubulars and confined concrete in compressive region
E_{scm} (MPa) = Elastic moment resisting modulus of joint at event I
$E_{scm}I_{sc0}$ = Composite bending rigidity of joint at state I
$f(\beta)$ = Influence coefficient of height to thickness ratio of column section on elastic bending rigidity of joint
H (mm) = Height of column
H_b (mm) = Height of beam cross section
H_f (mm) = Width of steel tube of limbs vertical to beam
H_{w1}, H_{w2} (mm) = Widths of flange 1 and 2
I_c (mm^4) = Moment of inertia of confined concrete
I_s (mm^4) = Moment of inertia of special shaped steel tube
I_{sc} (mm^4) = Modified composite moment of inertia for joint
I_{sc0} (mm^4) = Composite moment of inertia for joint
k = Influence parameters of cross-section shape and height to thickness ratio of column section on shape characteristic of M_j-θ_r curves
K_e (kN·m) = Elastic bending rigidity of joint
L_w, L_f (mm) = Depths of steel tube of limbs parallel and vertical to beams
M_e, M_y (kN·m) = Bending moments at state points I and II
M_j (kN·m) = Bending moment of panel zone
M_{uj} (kN·m) = Ultimate bending moment of joint
N (kN) = Axial pressure force on top of column
N (kN) = Load applied to column
n = Axial compression ratio of column

n_s = Parameter related to shape of M_j-θ_r curves
p (N/mm^2) = Constraint reaction stresses on steel tubes of limbs parallel and vertical to beams
p_{cw}, p_{cf} (N/mm^2) = Tightening-ring stresses of confined concrete in effective constraint region of limbs parallel and vertical to beams
p_e (N/mm^2) = Equivalent tightening-ring stresses of confined concrete in model of equivalent concrete-filled circular steel tube
p_{ecw}, p_{ecf} (N/mm^2) = Equivalent tightening-ring stresses of confined concrete in effective constraint regions of limbs parallel and vertical to beams in model of equivalent concrete-filled circular steel tubular
p_{hf}, p_{vf} (N/mm^2) = Horizontal and vertical constraint reaction stresses on steel tubes exerted by confined concrete in limbs vertical to beam
p_{hw}, p_{vw} (N/mm^2) = Horizontal and vertical constraint reaction stresses on steel tube exerted by confined concrete in limb parallel to beam
Q (kN) = Intersection point between starting point of para-curve corresponding to web limb and y-axis
S (mm^2) = Ineffective restraint area of confined concrete
t_b, t_d (mm) = Thicknesses of flanges of beam and internal diaphragm
t_{f1}, t_{f2} (mm) = Thicknesses of flanges of limbs parallel and vertical to beams
t_{w1}, t_{w2} (mm) = Thicknesses of steel webs of limbs parallel and vertical to beams
u = Neutral axis of column section
V (kN) = Lateral load on top of column
α_1 = Ratio of steel content of limb parallel to beam
α_2 = Ratio of steel content of limbs vertical to beam
α_E = Ratio of modulus elastic of steel tube to that of confined concrete
α_{s1}, α_{s2} = Stiffness reduction ratios at yield point and plastic stiffness reduction point
β = Height to thickness ratio of column section
γ = Ratio of moment of inertia of steel tube to that of confined concrete
δ = Relative angle between plastic hinges at beam and column ends
δ_m (mm) = Horizontal displacement of panel zone
δ_u (mm) = Horizontal displacement of column
θ_b = Rotation of beam end
θ_c = Rotation of column end
θ_e, θ_y, θ_r = Rotations at state points I, II and III
θ_e = Reference rotation which is ratio of ultimate bending moment of joint to elastic bending rigidity of joint
θ_r = Relative rotation between ends of column and beam
λ = Ratio of sectional area of steel tube to that of confined concrete
ξ = Confinement coefficient of whole unified material constituted by limbs parallel and vertical to beams
ξ_f = Confinement coefficient ξ_f of limbs vertical to beam
ξ_w = Confinement coefficient of limb parallel to beam
σ_{cB} (N/mm^2) = Axial compressive strength of confined concrete
σ_{sw}, σ_{sf} (N/mm^2) = Transverse tension stresses of steel webs of limbs parallel and vertical to beams
σ_{sy}, σ_{sr}, σ_{sB} (N/mm^2) = Stress at yield point, plastic stiffness reduction point, and ultimate point
φ = Initial angle of para-curve at intersection point

ORCID

Xi Chen http://orcid.org/0000-0002-0961-7264
Hechao Li http://orcid.org/0000-0003-0301-8225
Guangxu Tu http://orcid.org/0009-0005-7398-0307
Xin Lu http://orcid.org/0000-0001-9527-8109

References

Abbas H, Siddiqui NA, Khateeb BM, Almusallam TH, Al-Salloum YA (2021) Performance of new CFST square column-to-foundation connections for cyclic loads. *Journal of Constructional Steel Research* 185:106868, DOI: 10.1016/j.jcsr.2021.106868

Cao JJ, Packer JA, Yang GJ (1998) Yield line analysis of RHS connections with axial loads. *Journal of Constructional Steel Research* 48:1-25, DOI: 10.1016/S0143-974X(98)90143-2

CECS159:2004 (2004) Technical specification for structures with concrete-filled rectangular steel tube members. China Architecture & Building Press, Beijing, China, 27-38 (in Chinese)

Chen X, Xue JY, Li HC, Lu X, Tu GX (2023) Elastoplastic analysis of shear resistance of special-shaped concrete-filled steel tubular connection. *Journal of Constructional Steel Research* 201:107712, DOI: 10.1016/j.jcsr.2022.107712

Cheng Y, Yang YL, Liu JP, Nie WQ, Chen YF (2023) Seismic performance and design method of T-shaped CFST column to U-shaped steel-concrete composite beam joint with vertical stiffeners. *Engineering Structures* 275:115270, DOI: 10.1016/J.engstruct.2022.115270

GB/T 228.1-2010 (2010) Metallic materials-tensile testing - part 1: method of test at room temperature. China Architecture & Building Press, Beijing, China, 1-19 (in Chinese)

GB/T 50081-2002 (2002) Standard for test method of mechanical properties on ordinary concrete. China Architecture & Building Press, Beijing, China, 4-15 (in Chinese)

Han LH, T Z, W WD (2009) Experiment, theory and methodology of modern composite and hybrid structures. Science Publishing Press, Beijing, China, 239-246 (in Chinese)

Khndada AE, Geschwindner LF (1997) Nonlinear dynamic analysis of steel frames by modal superposition. *Engineering Structures* 123(11):

1519-1527, DOI: 10.1061/(ASCE)0733-9445(1997)123:11(1519)

Liu WH, Guo YL, Tian ZH, Yang X, Li JY (2023) Experimental and numerical study of T-shaped irregularly concrete-filled steel tube columns under combined axial loads and moments. *Journal of Building Engineering* 65:105796, DOI: 10.1016/j.jobe.2022.105796

Liu XG, Liu JP, Yang YL, Cheng GZ, Joel Lanning J (2020) Resistance of special-shaped concrete-filled steel tube columns under compression and bending. *Journal of Constructional Steel Research* 169:106038, DOI: 10.1016/j.jcsr.2020.106038

Liu J, Zhou T, Lei ZY, Chen XD, Chen ZH (2019) Eccentric compression performance of slender L-shaped column composed of concrete-filled steel tubes connected by steel linking plates. *Journal of Constructional Steel Research* 162:1-16, DOI: 10.1016/j.jcsr. 2019.06.012

Mander JB, Priestley MJN, Park R (1988) Theoretical stress-strain model for confined concrete, *Journal of Structural Engineering* 114(8): 1804-1826, DOI: 10.1061/(asce)0733-9445(1988)114:8(1804)

Patel KV, Chen WF (1984) Nonlinear analysis of steel moment connections. *Journal of Structural Engineering* 110(8):1861-1874, DOI: 10.1061/(ASCE)0733-9445(1984)110:8(1861)

Qin Y, Chen ZH, Rong B (2015a) Component-based mechanical models for concrete-filled RHS connections with diaphragms under bending moment. *Advances in Structural Engineering* 18(8):1241-1255, DOI: 10.1260/1369-4332.18.8.1241

Qin Y, Chen ZH, Rong B (2015b) Modeling of CFRT through-diaphragm connections with H-beams subjected to axial load. *Journal of Constructional Steel Research* 114:146-156, DOI: 10.1016/j.jcsr.2015.04.015

Qin Y,Chen ZH, Wang XD (2014) Elastoplastic behavior of through-diaphragm connections to concrete-filled rectangular steel tubular columns. *Journal of Constructional Steel Research* 93:88-96, DOI: 10.1016/j.jcsr.2013.10.011

Shehab BA, Ekmekyapar T (2021) Joints behaviour of through steel beam to composite column connection: Experimental study. *Marine Structures* 76:1-23, DOI: 10.1016/j.marstruc.2020.102921

Wang WD, Han LH, Uy B (2008) Experimental behaviour of steel reduced beam section to concrete-filled circular hollow section column connections. *Journal of Constructional Steel Research* 64:493-504, DOI: 10.1016/j.jcsr.2007.10.005

Yang YL, Wang YY, Fu F, Liu JC (2015) Static behavior of T-shaped concrete-filled steel tubular columns subjected to concentric and eccentric compressive loads. *Thin-Walled Structures* 95:374-388, DOI: 10.1016/j.tws.2015.07.009

Yang YL, Wang GJ, Yang WQ, Wei X, Chen YF (2022) Experimental research on fire behavior of L-shaped CFST columns under axial compression. *Journal of Constructional Steel Research* 198:107505, DOI: 10.1016/j.jcsr.2022.107505

Zhang YB, Han LH, Zhou K, Yang ST (2019) Mchanical performance of hexagonal multi-cell concrete-filled steel tubular (CFST) stub columns under axial compression. *Thin-Walled Structures* 134:71-83, DOI: 10.1016/j.tws.2018.09.027

Zheng YQ, Pengsong Lai PS (2020) Experimental behavior of T-shaped concrete-filled steel tubular columns under diagonal cyclic loading. *Journal of Constructional Steel Research* 169:106037, DOI: 10.1016/j.jcsr.2020.106037

Zhong ST (2003) The concrete-filled steel tubular structures. Tsinghua University Press, Beijing, China, 61-83 (in Chinese)

Zhong ST (2006) The research and application of united design theory of concrete filled steel tube. Tsinghua University Press, Beijing, China, 37-77 (in Chinese)

Zhou GJ, An YH, Li DS, Ou JP (2019) Analytical model of moment-rotation relation for steel beam to CFST column connections with bidirectional bolts. *Engineering Structures* 196:1-11, DOI: 10.1016/j.engstruct.2019.109374